A Multi-Method Approach to Flood Mapping: Reconstructing Inundation Changes in the Cambodian Upper Mekong Delta

Christina Anna Orieschnig, Jean-Philippe Venot, Sylvain Massuel, Khy Eam Eang, Kong Chhuon, Sambo Lun, Siev Sokly, Gilles Belaud

A Multi-Method Approach to Flood Mapping: Reconstructing Inundation Changes in the Cambodian Upper Mekong Delta

Christina Orieschnig[a], Jean-Philippe Venot[b], Sylvain Massuel[b], Khy Eam Eang[c], Kong Chhuon[c], Sambo Lun[c], Sokly Siev[d], Gilles Belaud[b]

[a] *UMR Hydrosciences, AgroParisTech, University of Montpellier, IRD, 300 Av. du Professeur Emile Jeanbrau, 34090 Montpellier, France*
[b] *G-Eau, IRD, AgroParisTech, Institut Agro, Cirad, INRAE, University of Montpellier, 361 rue J.F. Breton, BP 5095, 34196, Montpellier Cedex 5, France*
[c] *Faculty of Hydrology and Water Resources Engineering, Institute of Technology of Cambodia, Russian Blvd., P.O. Box 86, Phnom Penh, Cambodia*
[d] *General Department of Science, Technology and Innovation, Ministry of Industry, Science, Technology and Innovation, 45 Preah Norodom Boulevard, Sangkat Phsar Thmey III, Khan Daun Penh, Phnom Penh 120203, Cambodia*

Abstract

As in many tropical deltas globally, annual floods shape the livelihoods of the largely rural population in the Cambodian Mekong delta. Agricultural cycles are keyed to the flood arrival, peak, and recession, and fish populations depend on inundated floodplains for their regeneration. However, as factors like climate change and hydropower infrastructure development are altering the Mekong's hydrology, the inundation dynamics of its deltaic floodplains are shifting as well. Several studies have assessed the general changes of river discharge and flood extent on a basin- or delta-wide scale. Yet the sustainable development of this region is relying on dynamics at more local and specific scales, which have not been addressed so far.

This paper presents a methodology to track the evolution of hydrological regimes and associated inundations in tropical deltas such as the upper Mekong delta in Cambodia, where it is applied over the past 30 years. Data scarcity and heterogeneity of the environment in this region necessitated the use of combined approaches. We established a link between water levels measured in-situ and

Email address: christina.orieschnig@ird.fr (Christina Orieschnig)

flood maps derived from optical and radar satellite images (Sentinel-1 and -2).The robustness of the link was assessed using Sentinel, Landsat imagery and the TanDEM-X (12m) elevation model. This water level-flood link (WAFL) was then used to reconstruct a daily time series of inundation extents reaching back to the beginning of hydrological measurements in 1991 (30 years). On this basis, changes in the incidence, duration, and spatial distribution of floods were analysed.

The results indicated that WAFL can be used to reconstruct inundation maps with an overall robustness of 87% in comparison to historical inundation maps derived from remote sensing imagery. Comparisons of WAFL-derived flood extents with Landsat images further underscored the significant role of local infrastructure, sedimentation dynamics, and land cover to explain changes in inundation dynamics. WAFL-based analyses revealed that inundation durations have decreased by an average of 19 days when comparing the periods before and after 2008, which was identified as a break point in the hydrological time series. Furthermore, a drastic decrease in inundation the annual frequency with which individual pixels are flooded can be detected during the first half of the traditional flood season, with an average of -21% in early August, negatively impacting water-based livelihoods, from agriculture to fisheries.

Keywords: Mekong delta, Cambodia, inundations, Sentinel-1 and -2, water levels

---

1. Introduction

Tropical deltas worldwide are fundamentally influenced by regional and local hydrological regimes (Kuenzer and Renaud, 2012; Loucks, 2019). Given low terrain gradients, inundation processes are central to their populations' water-based livelihoods. Yet it is often not well-understood what impact large-scale, basin-wide changes have on more local systems, often due to a lack of data. This is illustrated perfectly by the Cambodian Mekong Delta.

As the largest trans-boundary river in Southeast Asia, the Mekong plays a crucial role in the socioeconomic development of the region, with agriculture and fisheries highly dependent on its flow regime (Kondolf et al., 2018; Boretti, 2020; Kummu and Sarkula, 2008). However, recent years have seen considerable shifts in the Mekong's hydrology (Yun et al., 2020; Trung et al., 2020). Its seasonal hydrological regime, defined by a flood pulse - a strong unimodal flow pattern induced by the annual Monsoon precipitation - has altered in terms of timing and magnitude. On a basin-wide scale, numerous studies have traced the reasons for this to a variety of factors, especially hydropower development and climate change (Hecht et al., 2018; Lacombe et al., 2014; Yang et al., 2019; Yun et al., 2020; Li et al., 2017; Pokhrel et al., 2018). For example, Hoang et al. (2019) project that dry season flows in the basin will more than double as a result of hydropower development, while wet season flows will decrease by 16% by 2050. Similarly, Hoang et al. (2016) conclude that climate change will result in a decrease of wet season flows by 7%, and an increase in dry season flows by 33% by 2065.

These basin-wide changes have a particularly adverse impact on downstream hydro-ecological systems in the Cambodian and Vietnamese Mekong Delta (Intralawan et al., 2018; Yoshida et al., 2020). In these areas, the annual inundations[1] fundamentally shape the livelihoods of the local population. They deposit nutrient-rich sediments on the floodplains, benefiting flood-recession agriculture,

[1] This paper uses the terms "flood" and "inundations" synonymously.

contribute to the recharge of soil moisture and groundwater after the dry season months (Dang et al., 2018; Kondolf et al., 2018) and are crucial for the reproductive cycles of fish species, supporting one of the world's most productive systems of inland fisheries (Poulsen et al., 2004; Hortle, 2009; Winemiller et al., 2016). The floodplains of the Mekong are significantly impacted by shifts in the incidence, duration, and spatial patterns of annual inundations as a consequence of basin-wide hydrological changes. This mirrors the situation in other major deltas worldwide, such as the Ganges–Brahmaputra and Amazon deltas (Szabo et al., 2016; Singha et al., 2020).

These factors have mostly been studied at large scales, based on different hydrological and hydrodynamic models or on past series of remote sensing imagery (Heng et al., 2021; Try et al., 2020; Li et al., 2019; Shin et al., 2020; Mohammed et al., 2018; Burbano et al., 2020). However, each of the proposed modeling approaches comes with its own limitations and simplifying assumptions, as well as with a challenge regarding parametrisation in these often relatively data-sparse regions of interest. In terms of remote sensing, freely accessible, consistent long-term image time series such as Landsat and MODIS can provide some insights into how the spatial patterns of inundations have shifted (Aires et al., 2020; Dang et al., 2016; Fayne et al., 2017). However, many of these series are limited in terms of the temporal and spatial resolution of images, and, in the case of optical images, exhibit data sparsity during the wet season due to cloud cover. They also have difficulties accounting for water areas dissimulated by natural vegetation. Due to the limitations inherent in each approach, the existing studies are unable to produce both sufficiently extensive time series and adapted spatial and temporal resolutions for analysing long-term flood dynamics at local scales. An alternative path is now available in the form of the Sentinel constellation by the European Space Agency (ESA). Its Sentinel-1 and 2 satellites, launched between 2014 and 2017 (Potin et al., 2019), provide freely available optical and SAR data, at a return period of five to six days and a spatial resolution of up to 10 m. This makes Sentinel a valuable basis to better understand dynamic hydrological processes, such as inundations, at local scales. Both Sentinel-1 and

-2 data have been widely used in hydrological applications, separately and in combination (Twele et al., 2016; DeVries et al., 2020; Tsyganskaya et al., 2018), including on delta floodplains (Quang et al., 2019; Singha et al., 2020; Pham-Duc et al., 2017). However, the disadvantage of the Sentinel series lies in its comparatively short duration, which makes it impossible to observe long-term trends.

The aim of the present paper is to present a new methodology to analyse long-term flood dynamics in data-sparse tropical deltas, in order to infer the impact of basin-wide hydrological alterations on local hydro-ecological systems. To circumvent barriers of data scarcity and limitations of any single method, we are proposing a novel multi-method approach to reconstruct a time series of daily inundation extents. The application of this approach is illustrated in the Cambodian upper Mekong delta, based on local water level measurements since 1991 and on Sentinel-derived flood maps.

Building on an in-depth qualitative understanding of international development relations and agricultural practices grounded in social sciences and acquired through interviews with farmers and key informants over the last five years (Venot and Jensen, 2021), the proposed solution is to link in-situ water levels with high-resolution inundation maps derived from Sentinel imagery to establish a water level - flood link (WAFL). On the basis of this link, daily inundation maps are reconstructed going back to 1991, and then used to assess changes in inundation incidences, durations, and spatial patterns. This approach helps overcome the paucity and heterogeneity of data available in the area. We further assess the robustness of the WAFL using comparisons with inundation extents and land cover parameters derived from Landsat imagery and the TanDEM-X (12 m) digital elevation model (Rizzoli et al., 2017; Hawker et al., 2019).

2. Study Area

Agriculture, fisheries and livelihoods of the Cambodian upper Mekong delta are deeply influenced by annual monsoon inundations, yet few studies so far have focused on understanding the hydrological dynamics of this area. With a few notable exceptions (Sothea et al., 2006; Heng et al., 2021; Orieschnig et al., 2021), studies have instead focused on the Vietnamese Mekong delta. However, the Cambodian side of the delta exhibits several striking differences to its Vietnamese counterpart - most importantly in terms of water control infrastructure. On the Vietnamese side of the border, an extensive dyke and sluice gate system allows considerable anthropogenic control over inundations (Park et al., 2020; Triet et al., 2017; Quoc Thanh et al., 2019). Such infrastructure is largely absent in the Cambodian part of the delta. Consequently, it can be conjectured that the effects of upstream alterations are more immediately evident in the inundation patterns of this region (Aires et al., 2020).

The study area is located 60 km south of the Cambodian capital Phnom Penh, on the banks of the Mekong and its distributary, the Bassac river. The Koh Khel and Neak Luong hydrological stations are located just north of the study area, on the Bassac and Mekong respectively. Furthermore, the Chau Doc and Tan Chau stations can be found a few kilometres south of the case study area, in Vietnam (see Figure 1).

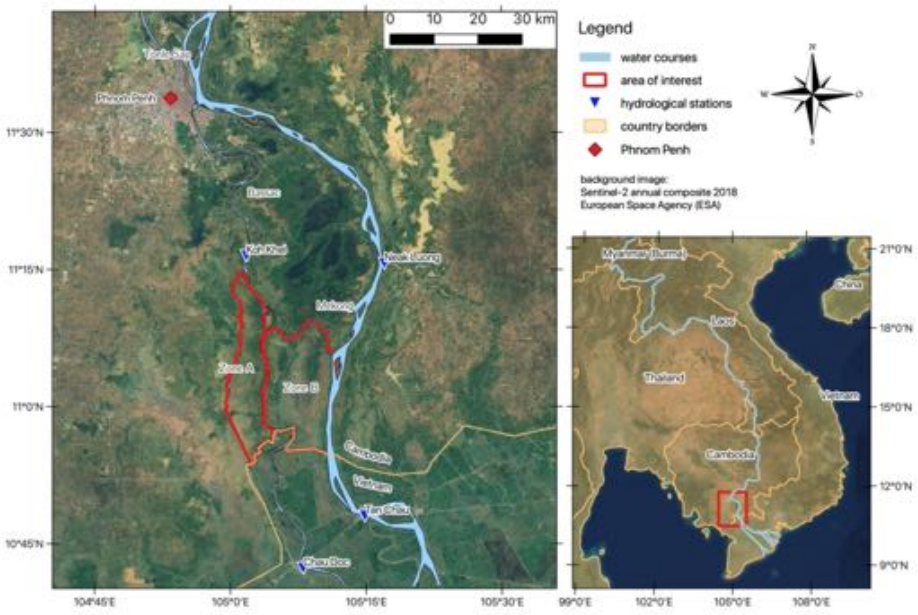

Figure 1: Geographic location of the study area in the Cambodian Mekong delta.

Given low levels of infrastructure development, especially when compared to Vietnam (Biggs, 2010), agriculture and fisheries in the case study area are inextricably keyed to inundation and precipitation dynamics. Typically, wet season precipitation begins in May, with river water levels rising in July to the point of inundating the floodplains. Floods extents usually peak in September and recede in late October and November. After the first rains and before the advent of the floods, farmers engage in what is locally called early wet season cultivation. Then, in the wake of the flood, they practice recession agriculture, harnessing the nutrient-rich sediments deposited during the flood and making use of residual soil moisture. Finally, some farmers engage in dry-season cultivation between March and May, using water stored in low-lying areas and the many drainage channels that crisscross the region (Khem, 2009; Vandôme, 2020; Venot and Jensen, 2021).

Floods are also crucial for small-scale capture fisheries, which provide an

essential component of the daily diet of the local population, and represent a significant share of the revenues of the poorest households in the region (Vilain et al., 2016). During the flood, fish populations regenerate on the floodplains (Hortle, 2009). Fish spawn either directly in the remaining expanses of inundated natural vegetation, or migrate from upstream in their juvenile stages to safely mature in the nutrient-rich shallow waters on the deltaic plains. When flood recession sets in, species migrate back to the main stream of the river, its distributaries, or smaller bodies of inland water, where they are later caught by local fishermen (Vu et al., 2021; Poulsen et al., 2004).

The study area is further divided into two sub-zones with different agricultural landscapes. The first region of interest (Zone A) is located on the right bank of the Bassac (see Figure 1). It encompasses a total area of 206.75 km^2. Its western and northern border are defined by a small distributary of the Bassac, its southern one by the Vietnamese border. Its landscape is characterised by Prek channels. These are human-made, trapezoidal channels, 10 to 50 meters wide and a few kilometers long, which diverge perpendicularly from the Bassac's main stream and connect it to low-lying floodplains by breaching the elevated river banks. In terms of agriculture, a gradient of cultivation can be observed along the length of each Prek. In areas that have been sufficiently raised by sediment deposition and are now rarely flooded (called *Chamkar*), high-value crops such as fruit trees and various vegetables are grown (Pinn et al., 2020).The further the terrain slopes away towards low-lying, regularly flooded areas (*Boeungs*), the more these crops give way to rice and maize.

The second area of interest (Zone B) is located on the opposite bank of the Bassac, and is bracketed between the Bassac in the West and the Mekong in the East (see Figure 1). In the North, it is limited by a canal and a dyke, in the South by the border to Vietnam. It covers an area of 312.65 km^2. This zone is characterized by a large interior floodplain, part of which feature man-made depressions, remnants of shallow reservoirs that were excavated during the Khmer Rouge period in the 1970s. Connecting these depressions to natural streams, a network of canals - also dug during the Khmer Rouge period and

re-excavated since then - spans across the area. Together, these structures support extensive areas of rice cultivation, with cropping calendars attuned to topography and flood timing. Recession rice, planted just after the flood, benefits from residual soil moisture and precipitation in December and January, which reduces the need for irrigation. A second rice crop, dry season rice, is sometimes planted between February and April, though the extent of this crop is usually limited by a lack of irrigation water, which needs to be pumped from canals and shallow reservoirs. Subsequently, early wet season rice is planted in late April or May. It is partially irrigated if water is available, but depends largely on the increased rainfall amounts in late April, May, and June. Typically, it is harvested just before the start of the flood in July.

When the timing, spatial patterns, and magnitude of inundations vary, specific problems result for agriculture, fisheries, and ecosystems in general (Nguyen et al., 2019). For instance, if floods arrive too soon, early wet season crops can be damaged or lost. In contrast, if inundations are shorter than expected, soil moisture and groundwater recharge can be insufficient, and reproduction times for fish populations are cut short. Similarly, a late flood recession can be problematic since it results in recession crops being planted with a delay, meaning flowering and harvesting may be negatively affected by dryer weather. Consequently, the need for irrigation is increased, which can cause issues given the lower water availability and higher overall production costs resulting from pump operation (Koponen et al., 2017). For these reasons, it is crucial to understand the spatial and temporal patterns of inundations in the area and their changes over the past decades.

3. Methodology

An overview of the methodology employed in this analysis is given in Figure 2.

The multi-method approach proposed in this paper is grounded in over five years of interdisciplinary research conducted by the authors. Through months

of collective field work, frequent interviews with multiple stakeholders, and in-situ water level measurements, the team acquired qualitative understanding regarding the development projects implemented in the area, local agricultural practices, and local hydrological processes. This understanding provided the context for the proposed approach, coupling remote sensing methods and hydrological analysis to study inundation trends in the Cambodian Upper Mekong delta.

First, an analysis of local hydrological trends and break points is carried out, to see if changes observed in the upper Mekong delta line up with basin-wide trends. Second, a water level - flood link (WAFL) is established. This is achieved by deriving a time series of inundation extents from Sentinel-1 and -2 imagery, and then linking them to locally measured water levels using a correlation model to take into account propagation delay times. As a third step, a time series of inundation extents is back-calculated on the basis of WAFL.

The robustness of the WAFL is assessed using Sentinel and Landsat images, as well as the TanDEM-X digital elevation model (12 m resolution). For one thing, WAFL-derived inundation extents are compared to inundation maps directly derived from Landsat and Sentinel-2. For another, they are compared to inundation extents derived from TanDEM-X. In addition, the effect of local land cover variables, especially natural vegetation such as shrubland and trees, on the inundation classification are evaluated using a land use land cover (LULC) classification based on Landsat images.

Finally, the changes in inundation incidences and durations in the Cambodian upper Mekong delta over the past three decades are quantitatively and qualitatively assessed according to break points derived from the hydrological analysis.

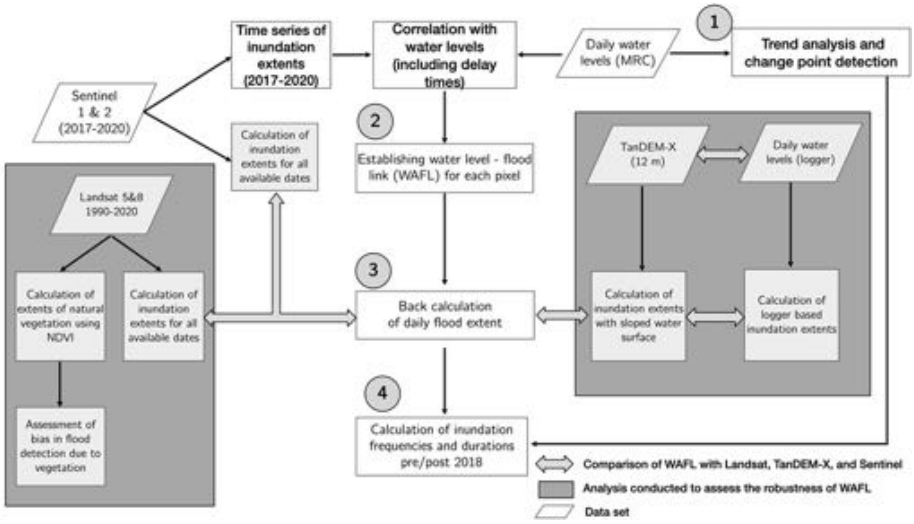

Figure 2: Overall analysis workflow

3.1. Hydrological Analysis: Identifying Trends and Change points

The hydrological analysis was carried out on the time series of water levels measured at four hydrological stations maintained by the Mekong River Commission (MRC). First a trend analysis was implemented using the non-parametric Mann-Kendall test (Hamed and Ramachandra Rao, 1998). Then, a change point detection was carried out using the Pettitt test (Pettitt, 1979), Buishand's range test (Buishand, 1982), and the standard normal homogeneity test (SNH, Alexandersson (1986)). This approach follows the analyses by Mallakpour and Villarini (2016), Yun et al. (2020), and Zhou et al. (2019). The parameters tested were the dates of the flood rise and recession, the overall flood duration, the duration of water levels above local thresholds, the average water level during the flood, and the maximum water level, along with the date at which it was reached each year (see Appendix A in supplementary materials for further explanations). All elevations are given in the local Ha Tien 1960 elevation datum.

The hydrological stations used in this analysis are Koh Khel and Chau Doc on the Bassac, and Neak Luong and Tan Chau on the Mekong (see Figure 1,

At Koh Khel, a continuous time series of daily water level measurements since autumn 1991 is available. At Neak Luong, a series is available since 1926, which is remarkably complete save for two larger gaps in 1946 and 1952-3. For this series, the tests were carried out twice: once on the entirety of the series, and once on a shortened series corresponding to the same duration as that available at Koh Khel. At both Chau Doc and Tan Chau series are available since 1980 and the analysis was conducted on the entirety of the series.

3.2. Detecting Flood Extents Using Sentinel-1 and 2

A series of flood maps was generated from SAR Sentinel-1 and optical Sentinel-2 images for the period 2017-2020. 2017 was chosen as a starting point because the satellite constellation was fully in place beginning that year. For this purpose, the series of Sentinel-1 and 2 images available on the cloud computing platform Google Earth Engine (Gorelick et al., 2017) was analysed. Past studies have illustrated the synergy effects for flood detection in combining both optical and SAR images, for Sentinel in particular (DeVries et al., 2020; Bioresita et al., 2019; Huang et al., 2002). Images were subjected to various pre-treatments. Sentinel-2 images were atmospherically corrected using the sen2cor algorithm (Main-Knorn et al., 2017) and clouds were masked based on the QA band. Sentinel-1 images underwent pre-processing based on the European Space Agency's Sentinel-1 toolbox. Metadata was updated with a restituted orbit file, border noise and thermal noise were removed, and radiometric calibration and orthorectification were applied. In addition, a refined Lee speckle filter (Lee, 1983) was implemented.

To classify each image into flooded and not flooded areas, three spectral indices were first calculated for the optical images: the Normalized Difference Vegetation Index (NDVI, Rouse J.W. et al. (1974)), the Normalized Difference Moisture Index (NDMI, Wilson and Sader (2002)) and the Normalized Difference Water Index (NDWI, McFeeters (1996)). For the optical images, these three indices were used as input bands for classification. For Sentinel-1, the VH and VV band were selected. On this basis, an unsupervised K-means classifi-

cation approach was chosen (Arthur and Vassilvitskii, 2007; Frank et al., 2016) to identify flooded areas in both Sentinel-1 and -2 images. This classification approach was selected because it can be applied equally to optical and SAR images, and because no local calibration of threshold values is required. As the training period for the classifier, a time window during the 2018 wet season - from September 25 to October 01 - was used due to the large flood extents and sharp contrast between open water and dry areas at this time. Validation of the flood classification was carried out using a total of 2340 points, set manually on the basis of SPOT-6 high-resolution imagery, on four different dates at different stages during the flood cycle: 2017/01/29, 2018/06/24, 2018/08/04, and 2019/01/27. On this basis, a confusion matrix and the kappa coefficient (Congalton, 1991) of the classification were calculated. This data was also used to determine the optimal number of clusters, which was determined to be two. After validation, the classifier was applied to the entire collection of Sentinel images, and the extents of open water areas were extracted for each image. Finally, the time series of inundation extents was exported, smoothed using a 3-day rolling mean, and scaled down to a daily time step using linear interpolation.

3.3. Establishing a Water Level - Flood Link (WAFL)

In the dynamics of inundations on large floodplains, a temporal lag is typically observed between the change in river water level and the change in flood extent (Zhang et al., 2017). Time is needed to fill the water bodies when the river flood occurs, accounting for a temporal lag between the flood dynamics and the river water levels. Similarly, the flood recession on the floodplains is out of phase with the river water level drop, since inundated areas decrease more slowly due to the retention of water by dykes and other floodplains structures. This results in hysteresis effects on the relationship between river water levels and the inundated surfaces (Hughes, 1980; Kummu et al., 2014). Lag times are controlled by the ease with which water can flow between the river and the floodplains, depending on hydraulic controls such as dykes, canals, bank heights, local topography, and water level gradients. Physically-based models

require geometric data of the main hydraulic connections and dykes, which are not accessible at this scale. Even high-resolution DEMs are often insufficient in terms of horizontal resolution and vertical accuracy to capture the hydraulic controls by dykes in the area, many of which are below 1 m in height. Due to the low terrain gradient, a water level rise of a few centimetres is enough to act as a tipping point for water to spill over certain dykes and induce several hectares of additional inundated surfaces. To account for this lag time, the correlative method for flood curves developed by Lamagat et al. (1993) was used (see Appendix B for more details).

Once the delay times had been made explicit, each inundation map was extracted from the time series of Sentinel-1 and 2 images and assigned a corresponding water level. Then, a flood count and water level link parameter were calculated for each pixel in the areas of interest. The approach used to achieve this is depicted in Figure 9 in Appendix C. The binary flood maps - flooded pixels having been assigned a value of 1 - were stacked. Subsequently, the sum of times each pixel was registered as flooded was calculated. As a result, pixels that represent permanent water areas, which are always detected as flooded, have a flood count equal to the number of images in the analysis. Pixels on elevated terrain areas that are never flooded have a flood count of zero. Next, flood counts are linked to water levels measured at Koh Khel. Each pixel was assigned the lowest water level (cm resolution) at which it was detected as being inundated.

3.4. Comparing the Flood Link With Inundation Extents Derived from Landsat and TanDEM-X

Since the link was established on the basis of relatively recent images from the second half of the 2010s, it became necessary to ascertain to which extent it was capable of delivering accurate estimates of inundated areas based on water levels from the 1990s and the 2000s. To this end, two approaches were chosen. The first was a comparison of inundation extents generated on the basis of the WAFL with those directly derived from Landsat images from the period 1991-

2020. The second was to use the TanDEM-X (12m) Digital Elevation Model (DEM), which is based on SAR imagery collected in the early 2010s, to generate estimates of flood extents and compare them with those generated on the basis of WAFL.

3.4.1. Comparison With Landsat

For the comparison with Landsat, a total of 94 optical Landsat-5 and -8 images were used.

To derive inundation maps from Landsat images, the same spectral indices as for Sentinel were calculated, and the images were then partitioned into flooded and dry areas by an unsupervised k-means algorithm. These maps were then compared with the inundation extents generated using the WAFL and the water level observed at the date the image was taken. First, the total inundated area was derived for each of the 94 images and compared to the calculated inundated area. Second, six Landsat images from flood seasons during the period of interest (1991-2020) were chosen to identify discrepancies in spatial inundation patterns. These images, at a time step of about five years, were selected because they provide rare cloud-free wet-season scenes. They date from 1991/11/29, 1995/11/05, 2000/08/31, 2005/08/21, 2013/09/12, 2015/09/11, and 2020/11/28.

3.4.2. Comparison Using TanDEM-X

A second method of testing the applicability of WAFL was to derive inundation maps from the TanDEM-X (12 m resolution) elevation model, provided by the German aerospace agency (Rizzoli et al., 2017). This DEM was used to assess the extent of inundation patterns as if they were solely linked to differences in detectable terrain elevation in the study area. To establish the comparison, flood extents were generated from the DEM by super-imposing a planar water surface onto the DEM and classifying all areas that were beneath the elevation of that surface as flooded. The planar water surface itself takes into account a North-South slope, based on water level measurements at Koh Khel and in-situ measurements at the western end of a Prek at the center of Zone A. Similar

to the Landsat measurements, a comparison of the size of inundated areas was carried out, along with spatially explicit comparisons of the distribution of inundations.

The comparison was also performed locally, directly based on in-situ measurements. The in-situ water level measurements were carried out using a differential pressure logger (Onset Hobo MX2001), with a complete time series available from September 2020 to April 2021 at 15-minute intervals. First, a pseudo water level in the floodplains within a radius of 1km of the logger was generated. This was achieved using inundation extents detected through Sentinel images, and the DEM-derived elevation-area curve of the zone, and based on the assumption that the water level is horizontal in such a small area (see Figure 20c in Appendix D). This pseudo water level was then compared with the levels measured in-situ. In reverse, the in-situ water level measurements were transformed into estimates of the size of the inundated areas within this 1 km radius around the logger, using the same curve. Finally, the inundation curves in this sub-area observed from Sentinel, and generated from WAFL and TanDEM-X were compared.

3.4.3. Land Use Classification: Detecting Natural Vegetation

A final element of the applicability of the WAFL related to the detection of natural vegetation in the area. Natural vegetation, such as shrubland and forests, can easily obscure open water surfaces due to canopy cover, especially in optical remote sensing imagery (Tsyganskaya et al., 2018; Pekel et al., 2016; Plank et al., 2017). To gauge the extent of this effect on the detection of inundations, an approach relying on a simple thresholding method using the NDVI was chosen. The NDVI was calculated for composite Landsat images for the dry seasons 1990/1991, 2000/2001, 2010/2011, and 2020/2021 for the months between March and May, which are the driest in the region. Then, areas exhibiting an NDVI of over 0.55 (Nath and Acharjee, 2013; Hashim et al., 2019) were classified as likely forest and shrubland. Further on in the analysis, the obscuring effect of canopy cover was taken into consideration by considering low-

lying areas classified as natural vegetation, which were otherwise surrounded by open water surfaces, as likely flooded.

3.5. Flood Dynamics Analysis: Calculating Inundation Durations and Incidences

As a next step, flood extent maps were used to generate inundation durations and incidences for each pixel (10 m) in the study area for the comparison periods identified on the basis of the hydrological time series. The term "inundation incidence" refers to the percentage of years in each of the two comparison periods during which any one pixel was flooded. Six different incidences were calculated: the overall annual inundation incidence (the % of years during the period that a given pixel is flooded, regardless of the date), along with inundation incidences at dates of interest to agricultural practices in the area, identified on the basis of interviews with stakeholders. These are the 15th of July, the 31st of July, the 15th of August (of importance for harvesting early wet season crops), the 31st of August, and the 25th of September (of importance for rainy season cultivation and planting of recession crops).

4. Results

4.1. Trends and Change Points in the Water Level Time Series

Detailed results of the analysis of hydrological trends and change points are given in Appendix D. The statistically significant trends that could be identified are highlighted in this section.

Generally, the water level time series at Koh Khel shows trends towards a later flood rise and an earlier flood recession (the latter is significant at $p < 0.1$). Most significant is the decrease of the duration of water levels at over 4 m[2] ($p = 0.022$). A break point is detected by all three homogeneity tests for the hydrological year 2007/08.

[2] A local threshold of 4 m rather than 5 as at Neak Luong was used here because there were several years in the time series when water levels did not exceed 5 m at all.

The water level series at Neak Luong since 1926 exhibits significant trends towards a later flood arrival ($p=0.03$), decreasing maximum water levels ($p<0.001$), and decreasing flood durations at over 5 m ($p<0.001$). The short time series (1990-2020) shows a trend towards an earlier flood recession ($p=0.06$), a shorter flood duration ($p=0.09$), and especially a decreasing average water level during the flood ($p=0.03$), as well as a decrease in the incidence of water levels above 5 m ($p=0.03$). Significant break points were detected 17 years into the time series, which corresponds to the break 2009/10.

At both Tan Chau and Chau Doc, break points were detected for the hydrological year 2007/08. In addition, there is a significant decreasing trend in terms of maximum water levels and flood durations of over 2 m at Tan Chau ($p<0.001$).

Overall, it emerged from the analyses that the hydrological year 2007/2008 significantly separates two statistically homogeneous periods characterised by different flood durations, dates of flood rise and recession, and flood peaks. Consequently, we used the years pre- and post-2008 as comparison periods for the analysis of inundation extents reconstructed using the WAFL.

4.2. Detection of Inundation Extents

In total, 119 Sentinel-2 and 360 Sentinel-1 images, taken between 2017/01/01 and 2020/12/31 were processed. This means that, on average, one image is available every three days. An example of an inundation map derived from a Sentinel-2 image on the basis of the k-means classification is given in Figure 15 in Appendix E. The average accuracy of the classification of flooded areas lay at 96.5%, with a Kappa value of 0.785. Details are given in Table 3 in Appendix E. However, it must be mentioned that these values at least partly result from the fact that the validation data used was itself derived from remote sensing imagery. Though it was set on the basis of high-resolution imagery, and with first-hand knowledge of the study area in mind, the validation points were still only set in unambiguous areas. Consequently, areas such as flooded vegetation or inundated rice fields prior to planting that cannot be easily discriminated

as either flooded or not in satellite imagery are underrepresented, and their ambiguities missing from the validation results.

Dynamics of inundation extents in Zone A and B, detected on the basis of optical and SAR Sentinel imagery and in relation to water levels at Koh Khel, are shown in Figure 3. A good general correspondence between the dynamics of the two curves can be observed. A time delay between the dynamics of the water level curves and the response of the inundated areas can be clearly seen. Large inundated areas correspond to high water levels several days prior, justifying the use of the Lamagat model as explained in the previous section - its results are given in Appendix E in Figures 16 and 17 as well as Tables 4 and 5.

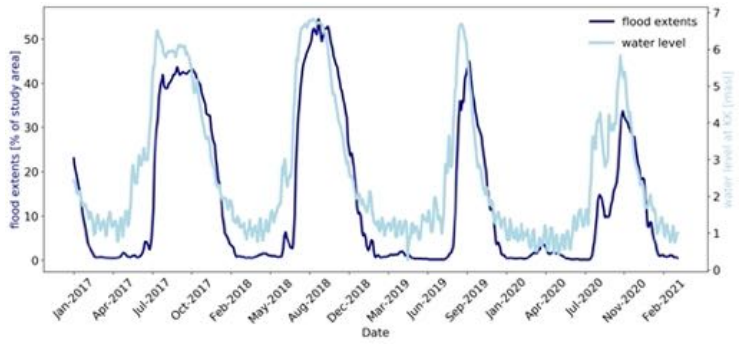

(a) Zone A

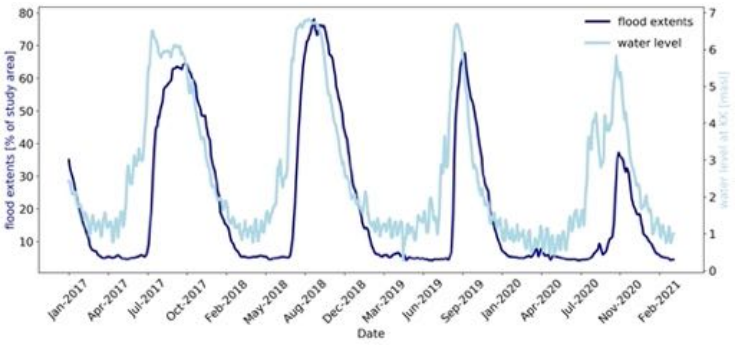

(b) Zone B

Figure 3: Dynamics of inundation extents and water levels measured at Koh Khel in the areas of interest 2017-2020.

4.3. The Water Level Flood Link (WAFL)

The water level flood link (WAFL) was calculated in accordance with the methodology described above. It is given in Figure 4, alongside the TanDEM-X elevation model. As can be seen, the WAFL shows similar elevation gradients to those seen in the DEM.

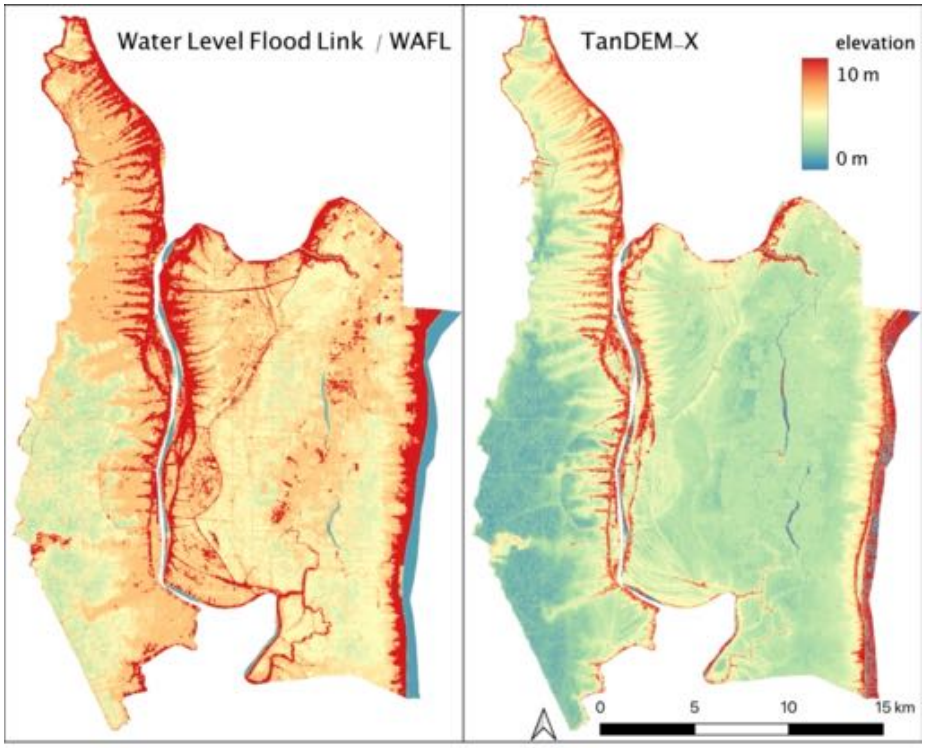

Figure 4: Side-by-side comparison of the water level at which each pixel becomes flooded, according to the WAFL, and the TanDEM-X terrain elevation model.

4.4. Comparison of Calculated Inundation Extents with Flood Maps Derived from Sentinel and Landsat and Influence of Natural Vegetation

In terms of comparing the inundation extents calculated using the WAFL with flood maps derived from Sentinel- and Landsat images, there is widespread agreement, though idiosyncratic variations remain.

The comparison of WAFL-calculated extents with Sentinel images showed an average classification agreement of 90.60% in images that were not obscured by clouds (see Figure 18 in Appendix F). The agreement between the calculated flood extents based on WAFL and those observed in the 94 Landsat images used in this analysis is shown in Figures 5 and 6, which shows the comparison for three specific dates. It emerges that in terms of overall inundated areas, there is a strong agreement between the two methods. As Figure 5 shows, there are some deviations in years that saw heavy floods, during which calculated inundation extents are lower than those obtained through Landsat classification.

In addition, it can be noted that the spatial distribution of inundations varies between the two methods of detection and that the deviations are more extensive the further back in time the points of comparison lie. For example, Figure 6 shows that WAFL-derived inundation maps detect extensive inundated areas in Zone B in the 2010s, while these areas are dry according to the Landsat classification. In contrast, areas of medium elevation in Zone A (transition zones between Boeung and Chamkar) appear as flooded in the 1990s and early 2000s in Landsat images, but are registered as dry by WAFL. The strong agreement between the total water surfaces obtained by the two methods may thus be contingent. This hypothesis will be further investigated in the discussion section.

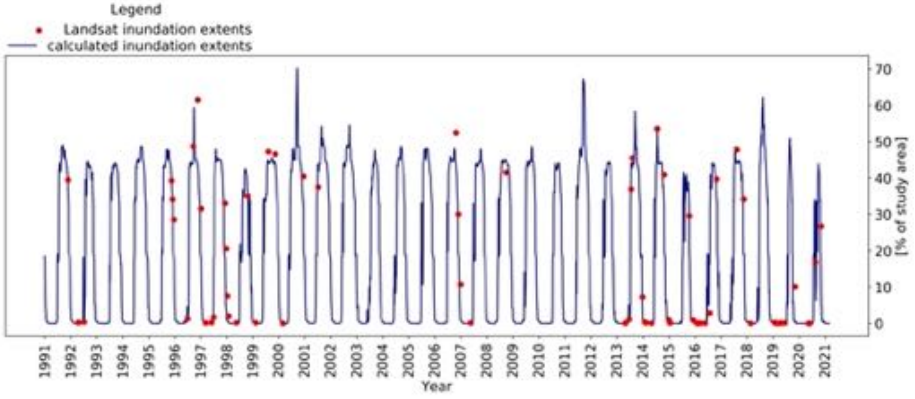

(a) Zone A

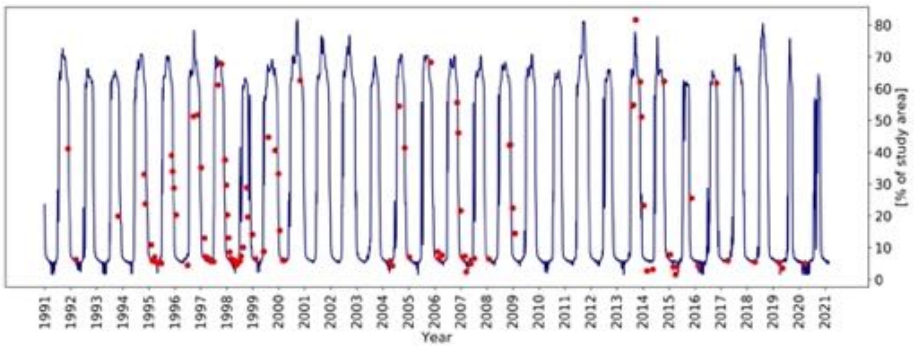

(b) Zone B

Figure 5: Comparison of inundated areas - time series derived from the WAFL, and individual Landsat-5 and -8 images

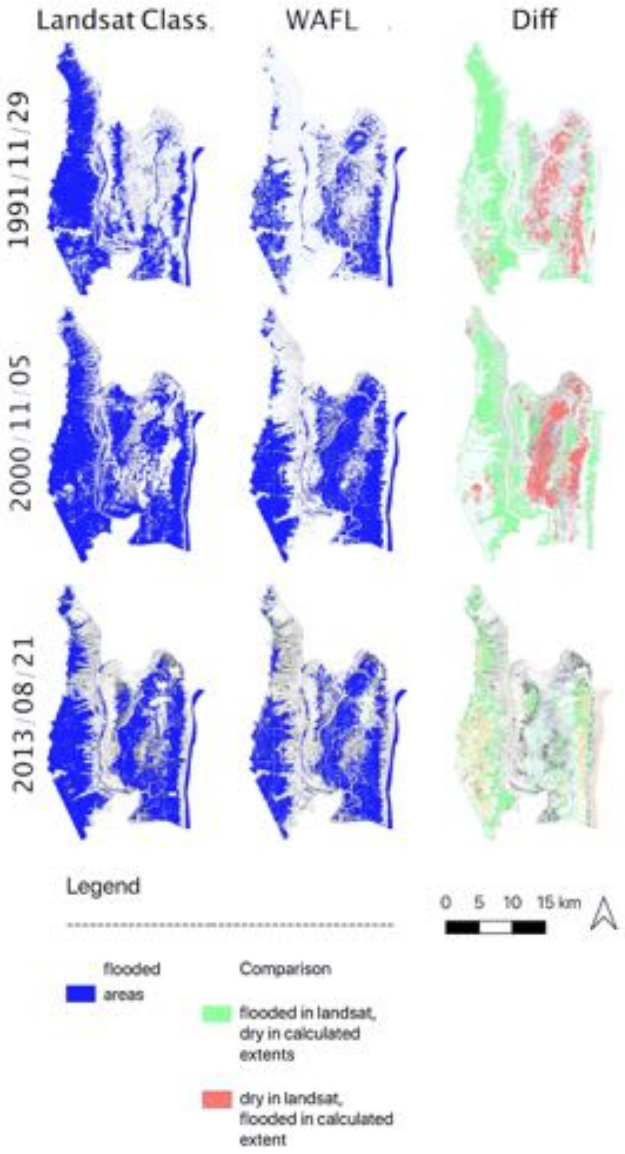

Figure 6: Comparison of inundation extents derived from the WAFL and Landsat-5 and -8 images

The analysis of the extents of natural vegetation indicates that extensive areas of shrubland and regularly flooded forests were present in Zone B in the

1990s, but that they shrunk to a fraction of their former size by 2020 due to large-scale conversion to rice fields. The decrease between 1990 and 2000 is limited, at ca. 2% of the overall area (see Figure 19 in Appendix F). After that, there is a sharp decline: -42% and -62% by 2010 and 2020 when compared to 1990. Such findings are supported by interview data.

In Zone A, the development is different. Here, natural vegetation detected in the early 1990s is located in the southwestern part of the study area. This patch of vegetation decreased considerably between 1990 and 2000 - by 64% in fact - due also to conversion to rice fields. After that, the overall extents of detected natural vegetation rebounded and even gained 20% in area in comparison to 1990. However, the increased extent of the detected natural vegetation is more likely to be due to the planting of fruit trees such as mango, whose areas, according to interviews and agricultural statistics, have sharply increased over the last 10 years.

Furthermore, the analysis of the extents of natural vegetation shows that there is an extensive overlap between those areas that are detected as flooded in WAFL-derived maps, but not by those generated directly from Landsat images. The Overlap line of Table 1 shows that upwards of 93% of pixels that exhibit these discrepancies coincide with the detected extents of natural vegetation. This indicates that these areas may be flooded but their water surface masked by canopy cover and hence not detected by Landsat imagery. If one considers that all forest pixels that overlap with areas being detected as dry by Landsat and wet by the WAFL are indeed flooded, agreement scores between the two methods for detecting flood extents increase from an average of 79.75% to 87.16% for Zone A, and from 68.49% to 87.18% for Zone B.

	Zone	1991	1995	2000	2005	2013	2015	2020
Agreement between LS and WAFL	A	67.64	68.85	74.98	81.85	85.68	85.87	93.37
[% of study area]	B	72.25	49.14	57.49	53.08	78.35	78.00	91.11
LS Wet - WAFL Dry	A	25.83	16.14	20.03	8.71	6.09	8.41	4.37
[% of study area]	B	6.93	14.68	19.76	11.06	8.9	20.13	7.37
LS Dry - WAFL Wet	A	6.53	15.00	4.99	9.44	8.22	5.72	2.25
[% of study area]	B	20.82	36.19	22.75	35.87	12.75	1.86	1.50
Overlap of LS dry area with forest	A	99.93	99.93	99.93	99.93	97.09	99.93	99.89
[% of dry area]	B	99.97	99.97	99.97	99.97	93.42	99.95	99.96
Corrected agreement	A	74.17	83.84	79.97	91.28	93.66	91.59	95.62
[% of study area]	B	93.06	85.32	80.23	88.94	90.26	79.86	92.61

Table 1: A comparison of the agreement and discrepancies between the WAFL-derived inundation extents (WAFL) and the Landsat-derived flood maps (LS).

4.5. Comparison of Calculated Inundation Extents with Flood Maps Derived from TanDEM-X

When it comes to the flood extents derived from TanDEM-X and their comparison with the inundation maps created using the WAFL, several salient points can be observed.[3] The comparison between TanDEM-X derived inundation maps in the 1-km radius around the in-situ sensor in Zone A and direct inundation observations from Sentinel images reveals a very good correspondence (see Figure 21 in Appendix F). Some hydraulic elements, like dykes, do not appear in TanDEM-X. This leads to an overestimation of flooded areas with the DEM compared to WAFL. We can also expect that these elements slow the filling of the area, introducing some delay between the water level measured at the sensor and the response in terms of inundations.[4] In addition, it emerges that the WAFL underestimates flood extents in this particular part of the study area in comparison to both the Sentinel-derived flood extents and those calculated from the TanDEM-X.

At a larger scale, the quality of this correspondence decreases, which illustrates the limitation of the DEM (especially to capture hydraulic connections and barriers) and of the assumption of a planar water surface. We can also

[3] See Figure 20 in Appendix F for the elevation-area curves extracted from TanDEM.

[4] This can be observed in Figures 22a and 22b in Appendix F, which show a lag time of a few days between the two curves.

513 expect errors due to propagation times not being evenly distributed throughout
514 the area.

515 The water level at which pixels become flooded according to the WAFL is
516 generally higher than their elevation in the TanDEM-X model (see Figure 4).
517 The exception to this is the center of Zone B. Here, the WAFL shows some
518 areas that become flooded at higher water levels than the surrounding terrain,
519 while the TanDEM-X registers continually low elevations.

520 As a consequence of this discrepancy between the WAFL and TanDEM-X
521 elevations, TanDEM-X-derived flood extents are generally higher than those
522 calculated using the WAFL (see Figure 7), even when taking into account a
523 North-South slope of the water surface area.

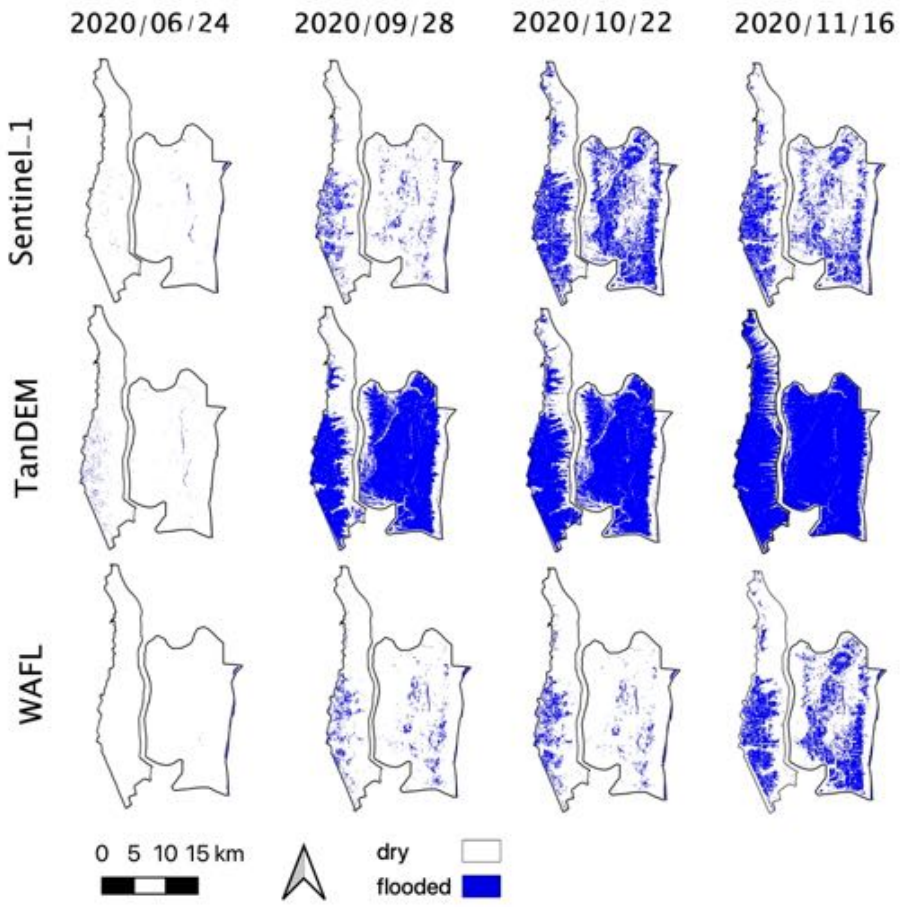

Figure 7: Comparison of inundation extents derived from TanDEM-X, and calculated from the WAFL, and as observed from Sentinel-1 for four dates during the 2020 flood season.

4.6. Changes in Inundation Incidence, Durations, and Patterns Pre- and Post-2008

When the WAFL is applied to the entirety of the water level time series to generate inundation maps, several trends emerge for the comparison periods 1991-2008 and 2009-2020. These trends are summarized in Table 2. It emerges that average annual inundation durations in both zones have decreased. In some areas of both zones, this decrease is as much as 39 days when the two periods are compared. In Zone A, the average decrease, at 15 days, was lower than in

Zone B, at 23 days.

As for inundation incidence, a similar overall declining trend can be noted. However, the magnitude of this decline is unevenly distributed across the flood season. Overall, there is a sharp decrease in inundation incidence in July and early August in both Zone A and B. In Zone A, the largest mean decrease, at -20% of years per period, can be observed in late July. In Zone B, this is the case for mid-August, at -23%. In contrast, the decrease in mean inundation incidence is limited in late September, a time at which the flood peak would traditionally have occurred already. At this time, the average inundation incidence remains unchanged in Zone B, and only declines by -8% in Zone A. On an annual basis, the decline in inundation incidence is much larger in Zone B, at -6% than in Zone A at -2%.

Parameter		Pixel-based changes in inundation incidence [% of years/period]						Changes in inundation duration [days]
		Jul 15	Jul 31	Aug 15	Aug 31	Sep 25	Overall	
Zone A	Max +	5	5	5	20	15	12	4.81
	Mean	-19	-20	-18	-16	-8	-2	-15.21
	Max -	-53	-41	-64	-33	-38	-25	-39.25
Zone B	Max +	5	5	5	15	15	12	5.17
	Mean	-13	-11	-23	-7	0	-6	-22.97
	Max -	-51	-48	-43	-35	-38	-30	-39.14

Table 2: Average changes in inundation incidence and durations in Zone A and B pre- and post-2008 for individual pixels. Given are the largest increase in flood incidence and duration for any individual pixel in the study area (Max +), the largest decrease for the same (Max -), as well as the average change in incidence and duration across all pixels in the study area.

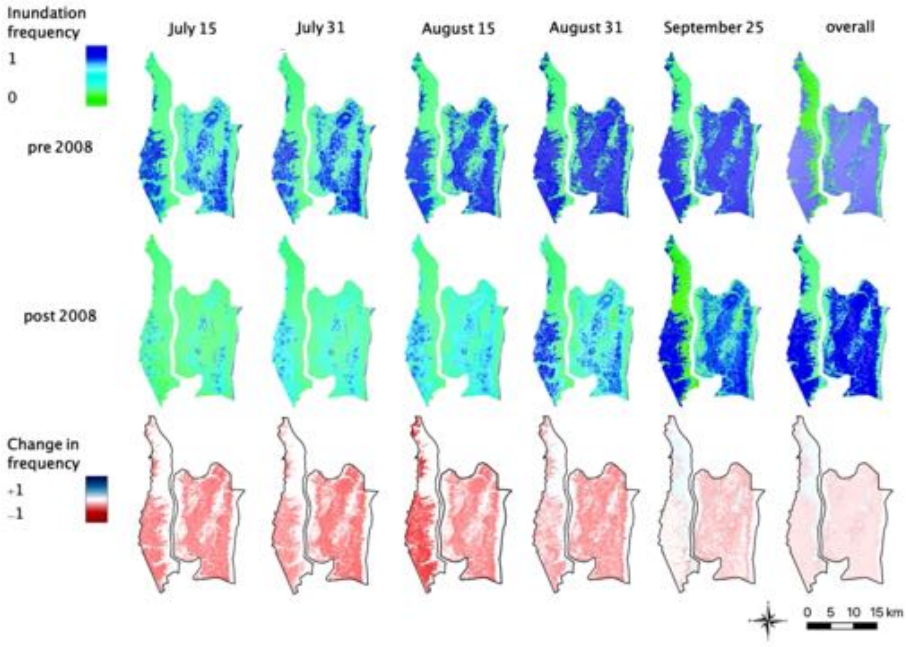

Figure 8: Visual comparison of inundation incidences pre- and post-2008

5. Discussion

5.1. Local Hydrological Trends and their Reflection of Basin-Wide Changes

Hydrological trends in the Cambodian upper Mekong delta closely mirrored those observed in basin-wide studies, with shorter flood durations and lower wet season water levels. Furthermore, the division of comparison periods into a pre- and post-2008 series mirrors the break point found in basin-wide studies, such as Yun et al. (2020) and Heng et al. (2021).

5.2. Inundation Mapping Using Sentinel: Between Biases and the Value of Observing Local Dynamics

In terms of inundation dynamics, curves of flood extents closely correspond to those of locally measured river water levels, both for Zone A and B. The most noticeable difference between the two zones is that the delay time between the two curves is longer for Zone B than for Zone A, which may be due to its

larger width, as well as the relatively shorter length of the Preks connecting the river to the floodplains. In combination, these terrain characteristics mean that floods take longer to reach the center of Zone B than of Zone A.

5.3. Validity of the WAFL: Balancing Natural Vegetation, Sedimentation, and Terrain Correspondence

The comparison between WAFL-derived inundation extents and flood maps extracted from Sentinel-2 imagery reveals several advantages and drawbacks of the proposed methodology. The benefit of using the WAFL-reconstructed inundation extents are best exemplified in the case of the image taken during the 2018 flood season, shown in Figure 18 in Appendix F. The optical Sentinel-2 images at this date show several gaps, left by cloud masking. However, not all clouds were properly detected by the masking algorithm and those that remain are falsely classified as dry areas in the Sentinel-derived flood map, leading to inconsistencies with the WAFL classification. The drawbacks of the methodology are most clearly revealed in the image from the 2020 flood season. Here, it is visible that the agreement of the two flood classifications is considerably higher in Zone A than in Zone B. Particularly, the WAFL classification in Zone B fails to capture some of the areas detected as inundated in the Sentinel-2 images. This may be due to the fact that water level dynamics in this year deviated considerably from the previously observed norm, with an early peak followed by a lowering of levels, before abruptly rising again towards the season's main peak. It can be conjectured that the correlative relationship established to characterise the delay time between water levels and the response of inundated areas failed to adequately capture this development. Whether this is an isolated response is hard to assess, since similar early peaking patterns cannot be found anywhere else in the data.

In terms of which factors most impact the detection of floods and the applicability of the WAFL, natural vegetation emerges as the central element in the comparison with Landsat images. This is particularly apparent as the binary classification into flooded and not flooded areas that was chosen in this approach

limits the possibility of detecting flooded vegetation. Overall, the comparison with Landsat-derived inundation maps highlights the potential of the WAFL for re-constructing past inundation extents. In general, while the WAFL also has some issues mistaking areas with natural vegetation for dry areas, even when they are flooded, this misclassification is much less frequent than with Landsat. There are two main reasons for that. First, Sentinel-1 SAR (on the basis of which the WAFL was derived) has the capacity to detect water under vegetation layers (Tsyganskaya et al., 2018). And second, at the time the Sentinel images were recorded (2017-20) there was already much less natural vegetation in the study area than at the time that many of the Landsat images used in this study were taken (cf. Figure 19 in Appendix F).

A second discrepancy in the comparison with Landsat is observed on higher-lying terrain in the study area. Here, Landsat continually registers inundations in the 1990s and early 2000s, which the WAFL fails to capture. That may be due to the fact that at the time that the Landsat images were recorded, these areas actually were flooded regularly, but that by the time the Sentinel images were taken, this had changed. Some possible explanations for that could be the construction of local infrastructure (such as small dams and dykes), the natural deposition of sediments, or the raising of land through geotechnical projects (it is not rare to see farmers raising the level of their land to build houses or plant trees). The regular distribution of this discrepancy in flood prevalence between Landsat and WAFL-derived maps seems to speak more for the second option. In terms of sediment deposition on the floodplains of the Mekong delta, Hung et al. (2014) found an average annual deposition of 6.86 kg/m^2 in the Vietnamese Mekong delta in Tam Nong district in Dong Thap province. This corresponds to an annual increase of 6 mm in height. These deposition rates are likely to be higher on the Cambodian side of the border due to the absence of dams and dykes. According to Manh et al. (2014), deposition on the Cambodian floodplains is indeed up to six times higher than in Vietnam, ranging from 19 to 23% of the annual sediment load at Kratie, rather than the 1 to 6% deposited in the compartmentalised floodplains in Vietnam. However, this also highlights

one of the principal limitations of WAFL - that it uses recent data to re-construct past inundation extents. As the conjectured effect of sedimentation shows, this may lead to errors where terrain configuration has changed significantly over the past decades. As the likelihood of such significant changes invariably increases over time, this necessarily means that the likely robustness of WAFL-derived maps diminishes the further back in time it is applied.

When it comes to the comparison of the WAFL with TanDEM-X and the inundation extents derived on both bases, using a planar water surface superimposed on the DEM on the basis of in-situ water levels, seems to be a valid approach on a local scale. From a physical perspective, it appears that the water level registered by the logger could be construed to represent the inflow into the Boeung area, while the pseudo water level derived from Sentinel can be seen as the storage response, with local hydrological processes mirroring the dynamics of those of a reservoir (the Boeung) filling and emptying. This is typical for flood storage cells: the inflow-outflow is governed by the difference in levels between the main connection point and the mean level in the area. The delay is directly linked to the volume of water stored in the considered area and the flow rate. When there is no obstacle in the considered area, the delay is very short and water level can be considered as horizontal (propagation effects are not visible at a daily time step). When dykes limit the flow propagation, the filling of the area is made possible by small openings in dykes (usually made by farmers to irrigate their rice fields). Then it takes a longer time to fill the area. During flood recession, the processes are inverted: water level decreases rapidly in the Preks that are well-connected to the Bassac, while water is stored in the floodplains. Water is kept as long as possible in rice fields (by clogging the dykes) and recedes progressively by gravity (surface and subsurface drainage) and evapotranspiration.

However, the robustness of this approach diminishes considerably when applied at the scale of the entire study area. At this scale, the assumption of a horizontal water surface slope no longer holds. Even when superimposing a sloped water surface over the entire DEM and taking into account correla-

tions between the station at Koh Khel and the logger, the discrepancy remains high due to the complexity of the hydrological processes in the area. Broadly, this leads to an overestimation of inundated extents derived from TanDEM-X. However, the use of the DEM does have the advantage of absolutely removing the interference of natural vegetation, as evidenced by the discrepancies in the center of Zone B observed in Figure 7.

5.4. Decreasing Flood Incidence and Durations in the Cambodian Mekong Delta: Patterns and Impacts

Despite limitations in the detection of the full flood extents in the 1990s and early 2000s, the analysis clearly shows a pronounced decrease in the incidence and duration of floods, especially in July and the first half of August. Large swaths of the study area, which were regularly flooded during these months in the 1990s, now remain dry until the second half of August. Taken together with the trends of earlier flood recession and the shorter flood durations outlined above, this means that overall, inundations in the Cambodian Mekong delta arrive later and recede earlier.

To a certain extent, this is in line with previous basin-wide studies such as Yun et al. (2020) and Hecht et al. (2018) that investigated the impacts of climate change and hydropower development. Their main findings were that a lower wet season discharge was to be expected in the future as a result of these developments, along with a higher dry season discharge. In terms of inundations, however, these higher dry season discharges do not balance the lack of inundations during the wet season that are key for the ecological functioning of the floodplains. Similarly, the results are in line with observations by Aires et al. (2020), who found a declining trend in inundation extents in their analysis of the Vietnamese and Cambodian Mekong delta using MODIS data.The same study also found inundations to be delayed by about two weeks in the Cambodian part of the Mekong delta. The present study indicates a longer delay, which may be due to differences in both the time frame and the spatial resolution of the data used. Figure 8 indicates that the incidences with which pixels were

flooded in late July prior to 2008 are now only attained in late August or early September. Similar parallels exist in the work of Heng et al. (2021). In their modelling study of the Cambodian floodplains - one of the few taking this region as its focus - the authors conclude that total flood extent is projected to decline by 18% by 2040.

Overall, the alterations outlined above are anathema to the formerly predictable hydrological regime of the region, and are likely to have wide-reaching consequences for agriculture and fisheries. Greater variability in the dates of the flood arrival and its recession may, for instance, result in shifts in the planting and harvesting times for recession crops and an increased need for irrigation water (Erban and Gorelick, 2016). As far as fisheries are concerned, the later onset of floods and overall decrease in inundation durations limit the period during which fish populations can regenerate in the shallow waters on the floodplains (Hortle, 2009). Compounded with the decrease in natural vegetation, which provides valuable structural habitat features, this is likely to negatively impact fish population dynamics. Vu et al. (2021) showed a close correlation between the long-term decline in commercial fish catches and declining peak water levels in the Mekong delta. Furthermore, local-level data obtained by the authors from fishermen in the area show fish catch to be much lower in years when the water level at Koh Khel exceeds 4 m for a lower number of days. These changes in inundation extents and durations are likely to impact food security in the region. Burbano et al. (2020), for example, link the shorter flood durations in the Tonle Sap region and the Mekong delta floodplains to shifts in dietary protein from fish to meat, and, consequently, land use changes resulting from the need to accommodate cattle.

Shorter inundation durations and lower incidence also reduce the spatial and temporal extent of the terrestrial-aquatic interface that many regulating ecosystem services depend on. This includes processes such as pest regulation, nutrient deposition, and soil and ground water recharge (Brown and My Phung, 2010; Chen et al., 2011).

Furthermore the analysis also shows that, even though large changes have

occurred in the basin over the past three decades, the link between river water levels and inundation extents has remained relatively static. In contrast to the major changes in the hydrology of the Mekong river, its hydraulic connections to its Cambodian floodplains seem to have changed comparatively little, which may be related to the still limited development of water control infrastructure in the region. At this point, it is important to note the fact that the results presented in this study partially mirror those from analyses of basin-wide trends in discharge and water levels because the WAFL has been constructed on the basis of these water levels. The merit of the study, though, lies in illustrating the magnitude of these parallelisms, which depends on the unique terrain configuration of the floodplain and the hydraulic controls that determine the dynamics of inundation processes.

5.5. Generalizability and Transferability to other Case Study Areas

As stated above, the ultimate aim of the developed methodology is to provide long-term insights into the spatial dynamics of inundations in tropical deltas. Applying the approach to the Mekong delta showed that this is possible with acceptable average accuracies of 87% in comparison to historical inundation maps derived from Landsat. Such comparisons have also highlighted the limitations of the WAFL with regard to long-term changes in local terrain configuration, and the challenges posed by LULC characteristics such as the presence of natural vegetation.

For an application in other study areas, this means that a basic knowledge of changes in local conditions is a prerequisite for the development and application of the WAFL. An awareness of landcover dynamics - which can be assessed through historical LULC analysis - or significant shifts in terrain elevations and the river-floodplain connections, notably due to the construction of water control infrastructures, is crucial. It must also be noted that the WAFL is primarily applicable in areas where inundations are correlated largely with dynamics in river water levels. This refers to areas in which the influence of local precipitations and groundwater is limited and where there are few obstacles to the flow

of water into and out of the floodplain. This can be mostly the case in semi-arid places but also in tropical areas like in the Mekong delta, as demonstrated in this study by the comparison of water level dynamics and Sentinel-derived inundation extents. Where historical records of water levels are available, as a first step in the application of WAFL, such an analysis should be used to elucidate the applicability of the methodology. However, in areas where inundations are significantly correlated with processes such as local precipitation or groundwater logging, adjustments to the correlation model can be made by introducing new input variables, provided time-series are available.

6. Conclusion

This paper offers an innovative approach, combining multiple methods and types of data, to elaborate a water level-flood link (WAFL) on the basis of which past daily inundation extents can be reconstructed, as illustrated for the Cambodian upper Mekong delta with a time series starting in 1991. Combining remote sensing and statistical methods with an in-depth knowledge of hydrological processes and agricultural dynamics of the Cambodian upper Mekong delta acquired over several years of research makes it possible to surmount barriers posed by the paucity and heterogeneity of data in this region, and attain a better understanding of changes in inundation dynamics.

The water level - flood link (WAFL) is established on the basis of Sentinel-1 and 2 data collected between 2017 and 2020 and in-situ hydrological measurements. Its robustness is further tested through a comparison with Landsat-derived inundation maps and inundation extents calculated on the basis of TanDEM-X. The results show that the WAFL is capable of acceptably representing past flood extents. For one thing, it has a smaller propensity for mistaking flooded vegetation for dry areas than inundation maps derived from Landsat images. For another, it is based on actual physical observations and thus avoids overestimating inundation extents, a pitfall to which flood maps derived from superimposing a sloped water surface on TanDEM-X are prone.

Nonetheless, it must be noted that due to long-term changes in terrain configuration due to sedimentation, and the construction of local infrastructure, the robustness of the method diminishes the farther back in time it is applied. In terms of improving the approach, it is possible to envision an additional layer of correction of the Sentinel-derived maps on the basis of TanDEM-X to remove any remnants of vegetation interference, as well as the improvement of the water surface slope on the scale of the floodplains. Furthermore, a spatialisation of delay times could lead to more regionally adapted results. And finally, a correction based on long-term sedimentation rates is conceivable.

In the case study area in the Cambodian Mekong delta, the results show a small decrease in overall inundation incidence as well as a sharp decrease in inundation incidence at specific dates in July and the first half of August. The results furthermore indicate that inundations duration are on average 19 days shorter in the period 2008-2020 than in the period 1991-2008. Overall, this is likely to have considerable adverse impacts on agricultural cycles, fish reproduction, and regulating ecosystem services such as soil and ground water recharge.

Considering all the limitations outlined above, the WAFL offers a valuable path to reconstructing a consistent time series of inundation extents going back to the 1990s. For the purpose of assessing long-term changes in spatial inundation patterns this is invaluable - especially considering the alternatives of having only sparse amounts of contemporary optical data, data with insufficient spatial and temporal resolution, or no spatial data at all. The WAFL methodology is applicable to other similar areas in large floodplains, where inundated areas are directly correlated to the water level at a gauging station through hydraulic processes and where historical water level data is available. In some areas, however, long-term shifts and precipitation contributions may require some further developments to improve the methodology.

Declaration of Competing Interest

The authors declare that they have no known competing financial interests or personal relationships that could have appeared to influence the work reported in this paper.

Acknowledgements

The authors thank the French Development Agency (AFD) for its support through the COSTEA project, the Wat-Health project (FSPI-2021), and our esteemed colleagues at the Institute of Technology of Cambodia as well as the Royal University of Agriculture for their invaluable partnership and support during field work.

CRediT Author Statement

Christina Orieschnig: Conceptualisation, Methodology, Software, Validation, Formal Analysis, Writing - Original Draft, Writing- Review and Editing, Visualisation **Jean-Philippe Venot**: Conceptualisation, Methodology, Writing - Review and Editing, Supervision, Project Administration, Funding Acquisition **Sylvain Massuel**: Conceptualisation, Investigation, Resources, Writing - Review and Editing, Project Administration, Funding Acquisition **Khy Eam Eang**: Investigation, Resources **Kong Chhuon**: Investigation, Resources **Sambo Lun**:Investigation, Resources **Sokly Siev**:Investigation, Resources **Gilles Belaud**:Conceptualisation, Methodology, Writing - Review and Editing, Supervision

References

Aires, F., Venot, J.P., Massuel, S., Gratiot, N., Pham-Duc, B., Prigent, C., 2020. Surface Water Evolution (2001–2017) at the Cambodia/Vietnam Border in the Upper Mekong Delta Using Satellite MODIS Observations. Remote Sensing 12, 800. doi:10.3390/rs12050800.

Alexandersson, H., 1986. A homogeneity test applied to precipitation data. Journal of Climatology 6, 661–675. doi:10.1002/joc.3370060607.

Arthur, D., Vassilvitskii, S., 2007. k-means++: The advantages of careful seeding, in: Proceedings of the eighteenth annual ACM-SIAM symposium on Discrete algorithms, Society for Industrial and Applied Mathematics. pp. 1027–1035.

Bader, J.C., Belaud, G., Lamagat, J.P., Ferret, T., Vauchel, P., 2016. Modélisation de propagation d'écoulement entre lits mineur et majeur sur les fleuves Sénégal et Niger. Hydrological Sciences Journal , 1–20doi:10.1080/02626667.2016.1148815.

Belaud, G., Bercher, N., 2010. Calibration of a propagation model in large river using satellite altimetry Water and Energy Saving: A Novel Low-Cost Solution for Water Wells View project Solar Induced Fluorescence View project, in: 6th International Symposium on Environmental Hydraulics, pp. 23–25. doi:10.1201/b10553-143.

Biggs, D.A., 2010. Quagmire : Nation-building and nature in the Mekong Delta. University of Washington Press.

Bioresita, F., Puissant, A., Stumpf, A., Malet, J.P., 2019. Fusion of Sentinel-1 and Sentinel-2 image time series for permanent and temporary surface water mapping. International Journal of Remote Sensing 40, 1–24. doi:10.1080/01431161.2019.1624869.

Boretti, A., 2020. Implications on food production of the changing water cycle in the Vietnamese Mekong Delta. Global Ecology and Conservation 22, e00989. doi:10.1016/J.GECCO.2020.E00989.

Brown, P.R., My Phung, N.T., 2010. Pattern and dynamics of rodent damage to lowland irrigated rice crops in An Giang, Vietnam. International Journal of Pest Management 57, 67–76. doi:10.1080/09670874.2010.529954.

Buishand, T., 1982. Some methods for testing the homogeneity of rainfall records. Journal of Hydrology 58, 11–27. doi:10.1016/0022-1694(82)90066-X.

Burbano, M., Shin, S., Nguyen, K., Pokhrel, Y., 2020. Hydrologic changes, dam construction, and the shift in dietary protein in the Lower Mekong River Basin. Journal of Hydrology 581, 124454. doi:10.1016/J.JHYDROL.2019.124454.

Chen, C.F., Son, N.T., Chang, L.Y., Chen, C.C., 2011. Monitoring of soil moisture variability in relation to rice cropping systems in the Vietnamese Mekong Delta using MODIS data. Applied Geography 31, 463–475. doi:10.1016/J.APGEOG.2010.10.002.

Congalton, R.G., 1991. A Review of Assessing the Accuracy of Classifications of Remotely Sensed Data. Remote Sensing of Environment 37, 35–46. doi:https://doi.org/10.1016/0034-4257(91)90048-B.

Dang, T., Cochrane, T., Arias, M., 2018. Quantifying suspended sediment dynamics in mega deltas using remote sensing data: A case study of the Mekong floodplains. volume 68. doi:10.1016/j.jag.2018.02.008.

Dang, T.D., Cochrane, T.A., Arias, M.E., Van, P.D.T., de Vries, T.T., 2016. Hydrological alterations from water infrastructure development in the Mekong floodplains. Hydrological Processes 30, 3824–3838. doi:10.1002/hyp.10894.

DeVries, B., Huang, C., Armston, J., Huang, W., Jones, J.W., Lang, M.W., 2020. Rapid and robust monitoring of flood events using Sentinel-1 and Landsat data on the Google Earth Engine. Remote Sensing of Environment 240, 111664. doi:10.1016/J.RSE.2020.111664.

Erban, L.E., Gorelick, S.M., 2016. Closing the irrigation deficit in Cambodia: Implications for transboundary impacts on groundwater and Mekong River flow. Journal of Hydrology 535, 85–92. doi:10.1016/j.jhydrol.2016.01.072.

878 Fayne, J.V., Bolten, J.D., Doyle, C.S., Fuhrmann, S., Rice, M.T., Houser, P.R.,
879 Lakshmi, V., 2017. Flood mapping in the lower Mekong River Basin using
880 daily MODIS observations. International Journal of Remote Sensing 38, 1737–
881 1757. doi:10.1080/01431161.2017.1285503.

882 Frank, E., Hall, M.A., Witten, I.H., 2016. The WEKA Workbench.

883 Gorelick, N., Hancher, M., Dixon, M., Ilyushchenko, S., Thau, D., Moore, R.,
884 2017. Google Earth Engine: Planetary-scale geospatial analysis for everyone.
885 Remote Sensing of Environment 202, 18–27. doi:10.1016/J.RSE.2017.06.
886 031.

887 Hamed, K.H., Ramachandra Rao, A., 1998. A modified Mann-Kendall trend
888 test for autocorrelated data. Journal of Hydrology 204, 182–196. doi:10.
889 1016/S0022-1694(97)00125-X.

890 Hashim, H., Latif, Z.A., Adnan, N.A., Alam, S., 2019. Urban Vegetation Clas-
891 sification with NDVI Threshold Value Method With Very High Resolution
892 (VHR) PLEIADES Imagery. The International Archives of the Photogram-
893 metry, Remote Sensing and Spatial Information Sciences XLII-4/W16, 237–
894 240. doi:10.5194/isprs-archives-XLII-4-W16-237-2019.

895 Hawker, L., Neal, J., Bates, P., 2019. Accuracy assessment of the TanDEM-X
896 90 Digital Elevation Model for selected floodplain sites. Remote Sensing of
897 Environment 232, 111319. doi:10.1016/J.RSE.2019.111319.

898 Hecht, J., Lacombe, G., Arias, M., Dang, T., Piman, T., 2018. Hydropower
899 dams of the Mekong River basin: a review of their hydrological impacts.
900 Journal of Hydrology 568, 285–300. doi:10.1016/j.jhydrol.2018.10.045.

901 Heng, S., Horton, A., Hok, P., Chung, S., Koponen, J., Kummu, M., 2021.
902 The Cambodian Mekong floodplain under the future development plans and
903 climate change. Natural Hazards and Earth System Science 65, 1–25. doi:10.
904 5194/nhess-2021-65.

Hoang, L.P., Lauri, H., Kummu, M., Koponen, J., van Vliet, M.T.H., Supit, I., Leemans, R., Kabat, P., Ludwig, F., 2016. Mekong River flow and hydrological extremes under climate change. Hydrology and Earth System Sciences 20, 3027–3041. doi:10.5194/hess-20-3027-2016.

Hoang, L.P., van Vliet, M.T., Kummu, M., Lauri, H., Koponen, J., Supit, I., Leemans, R., Kabat, P., Ludwig, F., 2019. The Mekong's future flows under multiple drivers: How climate change, hydropower developments and irrigation expansions drive hydrological changes. Science of the Total Environment 649, 601–609. doi:10.1016/j.scitotenv.2018.08.160.

Hortle, K.G., 2009. Fisheries of the Mekong River Basin. The Mekong , 197–249doi:10.1016/B978-0-12-374026-7.00009-7.

Huang, C., Davis, L.S., Townshend, J.R.G., 2002. An assessment of support vector machines for land cover classification. International Journal of Remote Sensing 23, 725–749. doi:10.1080/01431160110040323.

Hughes, D.A., 1980. Floodplain inundation: Processes and relationships with channel discharge. Earth Surface Processes 5, 297–304. doi:10.1002/esp.3760050308.

Hung, N.N., Delgado, J.M., Güntner, A., Merz, B., Bárdossy, A., Apel, H., 2014. Sedimentation in the floodplains of the Mekong Delta, Vietnam Part II: deposition and erosion. Hydrological Processes 28, 3145–3160. doi:10.1002/hyp.9855.

Intralawan, A., Wood, D., Frankel, R., Costanza, R., Kubiszewski, I., 2018. Tradeoff analysis between electricity generation and ecosystem services in the Lower Mekong Basin. Ecosystem Services 30, 27–35. doi:10.1016/j.ecoser.2018.01.007.

Khem, S., 2009. Assessment of Double Rice Cropping in the Cambodian Mekong Delta using a Flood Inundation Model. doi:10.13140/RG.2.1.1899.8886.

Kondolf, G.M., Schmitt, R.J.P., Carling, P., Darby, S., Arias, M., Bizzi, S., Castelletti, A., Cochrane, T.A., Gibson, S., Kummu, M., Oeurng, C., Rubin, Z., Wild, T., 2018. Changing sediment budget of the Mekong: Cumulative threats and management strategies for a large river basin. Science of The Total Environment 625, 114–134. doi:10.1016/j.scitotenv.2017.11.361.

Koponen, J., Paiboonvorachat, C., Munoz, A., 2017. The Council Study: Study on the sustainable management and development of the Mekong River, including impacts of mainstream hydropower projects. Report on the Positive and Negative Impacts of Irrigation on the Social, Environment, and Economic Conditions of the Lower Mekong River Basin and Policy Recommendations. Technical Report. Mekong River Commission. Vientiane, Laos PDR. URL: https://www.mrcmekong.org/assets/Publications/Council-Study/Irrigation-report_Council-Study.pdf.

Kuenzer, C., Renaud, F., 2012. Climate Change and Environmental Change in River Deltas Globally, in: The Mekong delta system - Interdisciplinary analyses of a river delta. Springer, Dordrecht, pp. 7–48.

Kummu, M., Sarkula, J., 2008. Impact of the Mekong River Flow Alteration on the Tonle Sap Flood Pulse. Ambio 37, 185–192. doi:10.1579/0044-7447(2008)37[185:IOTMRF]2.0.CO;2.

Kummu, M., Tes, S., Yin, S., Adamson, P., Józsa, J., Koponen, J., Richey, J., Sarkkula, J., 2014. Water balance analysis for the Tonle Sap Lake-floodplain system. Hydrological Processes 28, 1722–1733. doi:10.1002/hyp.9718.

Lacombe, G., Douangsavanh, S., Baker, J., Hoanh, C.T., Bartlett, R., Jeuland, M., Phongpachith, C., 2014. Are hydropower and irrigation development complements or substitutes? The example of the Nam Ngum River in the Mekong Basin. Water International 39, 649–670. doi:10.1080/02508060.2014.956205.

Lamagat, J.P., Morel-Seytoux, H.J., Albergel, J., 1993. Analyse de la propagation des ondes de crues. Hydrologie Continentale 8, 113–137.

961 Leauthaud, C., Belaud, G., Duvail, S., Moussa, R., Grünberger, O., Albergel, J.,
962 2013. Characterizing floods in the poorly gauged wetlands of the Tana River
963 Delta, Kenya, using a water balance model and satellite data. Hydrology and
964 Earth System Sciences 17, 3059–3075. doi:10.5194/hess-17-3059-2013.

965 Lee, J.S., 1983. A simple speckle smoothing algorithm for synthetic aperture
966 radar images. IEEE Transactions on Systems, Man, and Cybernetics SMC-13,
967 85–89. doi:10.1109/TSMC.1983.6313036.

968 Li, D., Long, D., Zhao, J., Lu, H., Hong, Y., 2017. Observed changes in flow
969 regimes in the Mekong River basin. Journal of Hydrology 551, 217–232.
970 doi:10.1016/J.JHYDROL.2017.05.061.

971 Li, D., Zhao, J., Govindaraju, R.S., 2019. Water benefits sharing under trans-
972 boundary cooperation in the Lancang-Mekong River Basin. Journal of Hy-
973 drology 577, 123989. doi:10.1016/J.JHYDROL.2019.123989.

974 Loucks, D.P., 2019. Developed river deltas: are they sustainable? Environmen-
975 tal Research Letters 14, 113004. doi:10.1088/1748-9326/ab4165.

976 Main-Knorn, M., Pflug, B., Louis, J., Debaecker, V., Müller-Wilm, U., Gascon,
977 F., 2017. Sen2Cor for Sentinel-2, in: Bruzzone, L., Bovolo, F., Benediktsson,
978 J.A. (Eds.), Image and Signal Processing for Remote Sensing XXIII, Interna-
979 tional Society for Optics and Photonics. p. 3. doi:10.1117/12.2278218.

980 Mallakpour, I., Villarini, G., 2016. A simulation study to examine the sensitivity
981 of the Pettitt test to detect abrupt changes in mean. Hydrological Sciences
982 Journal 61, 245–254. doi:10.1080/02626667.2015.1008482.

983 Manh, N.V., Dung, N.V., Hung, N.N., Merz, B., Apel, H., 2014. Large-
984 scale suspended sediment transport and sediment deposition in the Mekong
985 Delta. Hydrology and Earth System Sciences 18, 3033–3053. doi:10.5194/
986 hess-18-3033-2014.

McFeeters, S.K., 1996. The use of the Normalized Difference Water Index (NDWI) in the delineation of open water features. International Journal of Remote Sensing 17, 1425–1432. doi:10.1080/01431169608948714.

Mohammed, I.N., Bolten, J.D., Srinivasan, R., Lakshmi, V., 2018. Satellite observations and modeling to understand the Lower Mekong River Basin streamflow variability. Journal of Hydrology 564, 559–573. doi:10.1016/j.jhydrol.2018.07.030.

Nath, B., Acharjee, S., 2013. Forest Cover Change Detection using Normalized Difference Vegetation Index (NDVI) : A Study of Reingkhyongkine Lake's Adjoining Areas, Rangamati, Bangladesh. Indian Cartographer 33, 348–353.

Nguyen, V.K., Pittock, J., Connell, D., 2019. Dikes, rice, and fish: how rapid changes in land use and hydrology have transformed agriculture and subsistence living in the Mekong Delta. Regional Environmental Change 19, 2069–2077. doi:10.1007/s10113-019-01548-x.

Orieschnig, C.A., Belaud, G., Venot, J.P., Massuel, S., Ogilvie, A., 2021. Input imagery, classifiers, and cloud computing: Insights from multi-temporal LULC mapping in the Cambodian Mekong Delta. European Journal of Remote Sensing 54, 398–416. doi:10.1080/22797254.2021.1948356.

Park, E., Ho, H.L., Tran, D.D., Yang, X., Alcantara, E., Merino, E., Son, V.H., 2020. Dramatic decrease of flood frequency in the Mekong Delta due to riverbed mining and dyke construction. Science of The Total Environment 723, 138066. doi:10.1016/J.SCITOTENV.2020.138066.

Pekel, J.F., Cottam, A., Gorelick, N., Belward, A.S., 2016. High-resolution mapping of global surface water and its long-term changes. Nature 540, 418–422. doi:10.1038/nature20584.

Pettitt, A.N., 1979. A Non-Parametric Approach to the Change-Point Problem. Applied Statistics 28, 126–135. doi:10.2307/2346729.

Pham-Duc, B., Prigent, C., Aires, F., 2017. Surface water monitoring within cambodia and the Vietnamese Mekong Delta over a year, with Sentinel-1 SAR observations. Water 9, 366. doi:10.3390/w9060366.

Pinn, T., Reach, S., Buntong, B., Acedo, A., 2020. Vegetable Farming Practices in Cambodia: Case study of Small-scale Vegetable Farmers in Kandal, Kampong Chhnang and Battambang Provinces. Journal of Environmental and Rural Development 11, 57–62.

Plank, S., Jüssi, M., Martinis, S., Twele, A., 2017. Mapping of flooded vegetation by means of polarimetric Sentinel-1 and ALOS-2/PALSAR-2 imagery. International Journal of Remote Sensing 38, 3831–3850. doi:10.1080/01431161.2017.1306143.

Pokhrel, Y., Burbano, M., Roush, J., Kang, H., Sridhar, V., Hyndman, D.W., 2018. A review of the integrated effects of changing climate, land use, and dams on Mekong river hydrology. Water 10, 266. doi:10.3390/w10030266.

Potin, P., Rosich, B., Miranda, N., Grimont, P., Shurmer, I., O'Connell, A., Krassenburg, M., Gratadour, J.B., 2019. Copernicus Sentinel-1 Constellation Mission Operations Status, in: IGARSS 2019 - 2019 IEEE International Geoscience and Remote Sensing Symposium, IEEE. pp. 5385–5388. doi:10.1109/IGARSS.2019.8898949.

Poulsen, A., Hortle, K., Valbo-Jorgensen, J., Chan, S., Viravong, S., Bouakhamvongsa, K., Suntornratana, U., Yoorong, N., Nguyen, T., Tran, B., 2004. Distribution and Ecology of Some Important Riverine Fish Species of the Mekong River Basin. Technical Report. Mekong River Commission. Phnom Penh.

Quang, N.H., Tuan, V.A., Hao, N.T.P., Hang, L.T.T., Hung, N.M., Anh, V.L., Phuong, L.T.M., Carrie, R., 2019. Synthetic aperture radar and optical remote sensing image fusion for flood monitoring in the Vietnam lower Mekong

basin: a prototype application for the Vietnam Open Data Cube. European Journal of Remote Sensing 52, 599–612. doi:10.1080/22797254.2019.1698319.

Quoc Thanh, V., Roelvink, D., van der Wegen, M., Reyns, J., Kernkamp, H., Van Vinh, G., Thi Phuong Linh, V., 2019. Flooding in the Mekong Delta: Impact of dyke systems on downstream hydrodynamics. Hydrology and Earth System Sciences 24, 189–212. doi:10.5194/hess-2019-64.

Rizzoli, P., Martone, M., Gonzalez, C., Wecklich, C., Borla Tridon, D., Bräutigam, B., Bachmann, M., Schulze, D., Fritz, T., Huber, M., Wessel, B., Krieger, G., Zink, M., Moreira, A., 2017. Generation and performance assessment of the global TanDEM-X digital elevation model. ISPRS Journal of Photogrammetry and Remote Sensing 132, 119–139. doi:10.1016/J.ISPRSJPRS.2017.08.008.

Rouse J.W., J., Haas, R., Schell, J., Deering, D., 1974. Monitoring Vegetation Systems in the Great Plains with ERTS, in: Freden, S.C., Mercanti, E.P., Becker, M.A. (Eds.), Third Earth Resources Technology Satellite-1 Symposium- Volume I: Technical Presentations NASA SP-351. NASA. volume 30103017, pp. 301–217.

Shin, S., Pokhrel, Y., Yamazaki, D., Huang, X., Torbick, N., Qi, J., Pattanakiat, S., Ngo-Duc, T., Nguyen, T.D., 2020. High Resolution Modeling of River-Floodplain-Reservoir Inundation Dynamics in the Mekong River Basin. Water Resources Research 56, e2019WR026449. doi:10.1029/2019WR026449.

Singha, M., Dong, J., Sarmah, S., You, N., Zhou, Y., Zhang, G., Doughty, R., Xiao, X., 2020. Identifying floods and flood-affected paddy rice fields in Bangladesh based on Sentinel-1 imagery and Google Earth Engine. ISPRS Journal of Photogrammetry and Remote Sensing 166, 278–293. doi:10.1016/J.ISPRSJPRS.2020.06.011.

Sothea, K., Goto, A., Mizutani, M., 2006. A Hydrologic Analysis on Inundation in the Flooding Area of the Mekong Delta, Cambodia: The Combined

Deterministic and Stochastic Models for Flood Forecasting, in: World Environmental and Water Resource Congress 2006, pp. 1–10. doi:10.1061/40856(200)213.

Szabo, S., Brondizio, E., Renaud, F.G., Hetrick, S., Nicholls, R.J., Matthews, Z., Tessler, Z., Tejedor, A., Sebesvari, Z., Foufoula-Georgiou, E., da Costa, S., Dearing, J.A., 2016. Population dynamics, delta vulnerability and environmental change: comparison of the Mekong, Ganges–Brahmaputra and Amazon delta regions. Sustainability Science 11, 539–554. doi:10.1007/s11625-016-0372-6.

Triet, N.V.K., Dung, N.V., Fujii, H., Kummu, M., Merz, B., Apel, H., 2017. Has dyke development in the Vietnamese Mekong Delta shifted flood hazard downstream? Hydrology and Earth System Sciences 21, 3991–4010. doi:10.5194/hess-21-3991-2017.

Trung, L.D., Duc, N.A., Nguyen, L.T., Thai, T.H., Khan, A., Rautenstrauch, K., Schmidt, C., 2020. Assessing cumulative impacts of the proposed Lower Mekong Basin hydropower cascade on the Mekong River floodplains and Delta – Overview of integrated modeling methods and results. Journal of Hydrology 581, 122511. doi:10.1016/J.JHYDROL.2018.01.029.

Try, S., Tanaka, S., Tanaka, K., Sayama, T., Lee, G., Oeurng, C., 2020. Assessing the effects of climate change on flood inundation in the lower Mekong Basin using high-resolution AGCM outputs. Progress in Earth and Planetary Science 7, 34. doi:10.1186/s40645-020-00353-z.

Tsyganskaya, V., Martinis, S., Marzahn, P., Ludwig, R., 2018. SAR-based detection of flooded vegetation – a review of characteristics and approaches. International Journal of Remote Sensing 39, 2255–2293. doi:10.1080/01431161.2017.1420938.

Twele, A., Cao, W., Plank, S., Martinis, S., 2016. Sentinel-1-based flood mapping: a fully automated processing chain. International Journal of Remote Sensing 37, 2990–3004. doi:10.1080/01431161.2016.1192304.

Vandôme, P., 2020. Agricultural vulnerability to hydrologic hazards in the prek area of the upper Mekong Delta, Cambodia. Technical Report. Montpellier SupAgro. Montpellier.

Venot, J.P., Jensen, C.B., 2021. A multiplicity of prek(s) : Enacting a socionatural mosaic in the Cambodian upper Mekong delta. Environment and Planning E: Nature and Space , 251484862110268doi:10.1177/25148486211026835.

Vilain, C., Baran, E., Gallego, G., Samadee, S., 2016. Fish and the Nutrition of Rural Cambodians. Asian Journal of Agriculture and Food Sciences 4, 2321–1571.

Vu, A.V., Hortle, K.G., Nguyen, D.N., 2021. Factors Driving Long Term Declines in Inland Fishery Yields in the Mekong Delta. Water 13, 1005. doi:10.3390/w13081005.

Wilson, E.H., Sader, S.A., 2002. Detection of forest harvest type using multiple dates of Landsat TM imagery. Remote Sensing of Environment 80, 385–396. doi:10.1016/S0034-4257(01)00318-2.

Winemiller, K.O., McIntyre, P.B., Castello, L., Fluet-Chouinard, E., Giarrizzo, T., Nam, S., Baird, I.G., Darwall, W., Lujan, N.K., Harrison, I., Stiassny, M.L.J., Silvano, R.A.M., Fitzgerald, D.B., Pelicice, F.M., Agostinho, A.A., Gomes, L.C., Albert, J.S., Baran, E., Petrere, M., Zarfl, C., Mulligan, M., Sullivan, J.P., Arantes, C.C., Sousa, L.M., Koning, A.A., Hoeinghaus, D.J., Sabaj, M., Lundberg, J.G., Armbruster, J., Thieme, M.L., Petry, P., Zuanon, J., Vilara, G.T., Snoeks, J., Ou, C., Rainboth, W., Pavanelli, C.S., Akama, A., Soesbergen, A.v., Saenz, L., 2016. Balancing hydropower and biodiversity in the Amazon, Congo, and Mekong. Science 351, 128–129. doi:10.1126/science.aac7082.

Yang, J., Yang, Y.E., Chang, J., Zhang, J., Yao, J., 2019. Impact of dam development and climate change on hydroecological conditions and natural hazard risk in the Mekong River Basin. Journal of Hydrology 579, 124177. doi:10.1016/J.JHYDROL.2019.124177.

Yoshida, Y., Lee, H.S., Trung, B.H., Tran, H.D., Lall, M.K., Kakar, K., Xuan, T.D., 2020. Impacts of Mainstream Hydropower Dams on Fisheries and Agriculture in Lower Mekong Basin. Sustainability 12, 2408. doi:10.3390/su12062408.

Yun, X., Tang, Q., Wang, J., Liu, X., Zhang, Y., Lu, H., Wang, Y., Zhang, L., Chen, D., 2020. Impacts of climate change and reservoir operation on streamflow and flood characteristics in the Lancang-Mekong River Basin. Journal of Hydrology 590, 125472. doi:10.1016/J.JHYDROL.2020.125472.

Zhang, W., Sun, W., Li, T., 2017. Uncertainties in the national inventory of methane emissions from rice cultivation: field measurements and modeling approaches. Biogeosciences 14, 163–176. URL: https://bg.copernicus.org/articles/14/163/2017/, doi:10.5194/bg-14-163-2017.

Zhou, C., van Nooijen, R., Kolechkina, A., Hrachowitz, M., 2019. Comparative analysis of nonparametric change-point detectors commonly used in hydrology. Hydrological Sciences Journal 64, 1690–1710. doi:10.1080/02626667.2019.1669792.

Appendix A: Explanation of the Choice of Hydrological Parameters Chosen for Analysis

These parameters reflect the immediate considerations of farmers with regard to their cultivation practices. The date of the flood arrival, for example, determines whether early wet season crops can be harvested in time, or whether they will suffer damage from the oncoming inundations. Similarly, the date of the flood recession dictates when crops can be planted on the formerly inundated fields and the extent to which they will depend on irrigation at the end of their growing cycle. The dates of the flood rise and recession - and thus the overall flood duration - were defined on the basis of the rate at which water levels rise and fall (Δwl). The date of the largest positive Δwl was taken as the start of the flood, the date of the largest negative Δwl as the date of recession. The number of days between these two dates was taken as the flood duration. Local water level thresholds were chosen on a qualitative basis, based on conversations with stakeholders. They reflect water depths that are conducive to fish reproduction and that farmers feel allow cultivation without constituting potential threats to harvesting.

Appendix B: The Lamagat Correlation Model

Initially developed to identify correlations between gauging stations, the Lamagat approach has been used with satellite data series in both the Tana river delta in Kenya by Leauthaud et al. (2013), and at the Niger and Senegal rivers by Bader et al. (2016) (flooded areas) and Belaud and Bercher (2010) (satellite altimetry). It was developed to model the propagation of flood waves, specifically in areas with low slope gradients and observable hysteresis effects in rating curves - such as deltaic floodplains. This approach combines kinematic elements with statistical methods. Its main advantage is that it identifies optimal correlation factors not between the overall time series of flood extents and water levels in the river, but between a set number of sub-sections of the time series. Consequently, it can account for the varying time delays depending on

the phase of the flood cycle. Therefore, the time delay is expressed as a function of the river water level, while the flood extent at a given time is a function of the water level observed some days before.

Appendix C: Visual Representation of WAFL Calculation

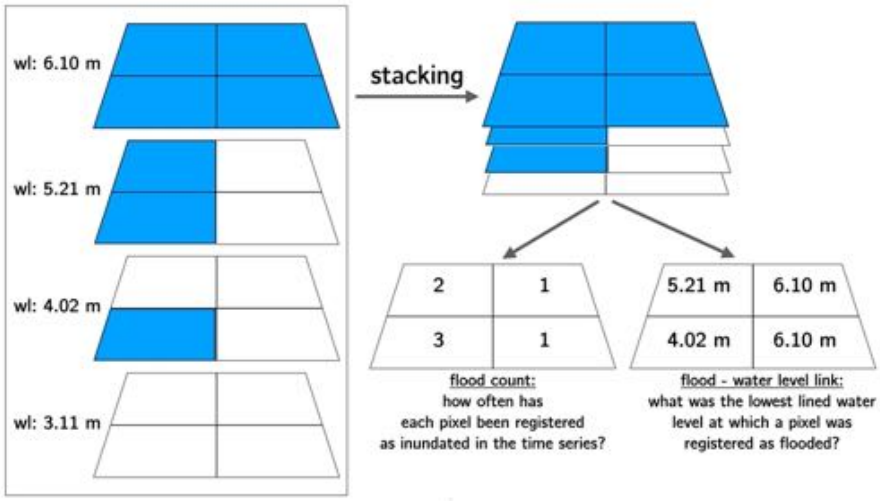

Figure 9: Logic workflow for creating the water level - flood link (WAFL). Example of an area with 4 pixels, and 4 images corresponding to 4 different water levels at Koh Khel. Blue areas represent flooded pixels.

Appendix D: Results of the Hydrological Analysis

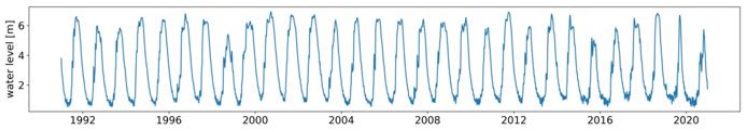

(a) Water levels at Koh Kehl 1990-present.

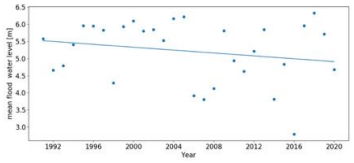

(b) Mean flood water levels at Koh Khel.

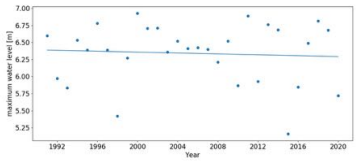

(c) Maximum water level at Koh Kehl.

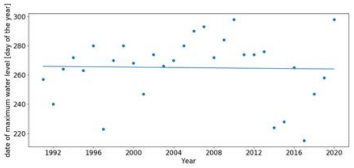

(d) Date of maximum water level at Koh Khel.

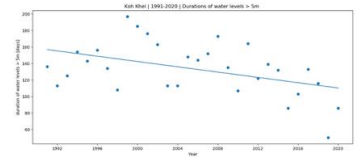

(e) Flood duration over 4 m at Koh Khel.

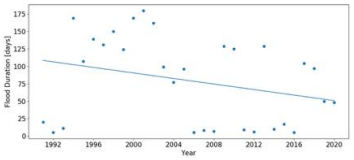

(f) Overall flood duration at Koh Kehl.

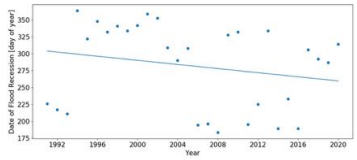

(g) Date of flood recession at Koh Khel.

Figure 10: Results of hydrological analysis at Koh Khel.

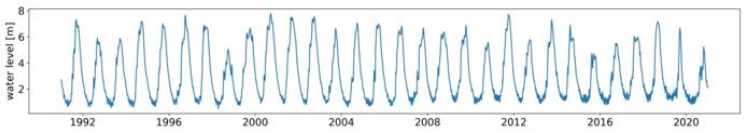

(a) Water levels at Neak Luong 1990-present.

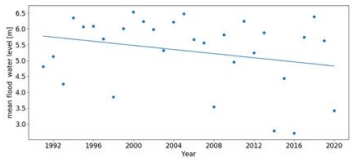

(b) Mean flood water levels at Neak Luong.

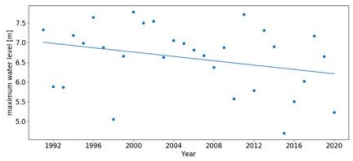

(c) Maximum water level at Neak Luong.

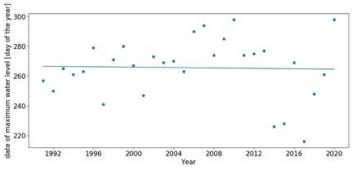

(d) Date of maximum water level at Neak Luong.

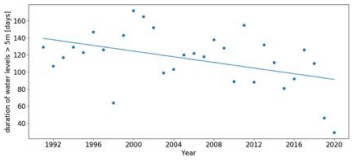

(e) Flood duration over 5 m at Neak Luong.

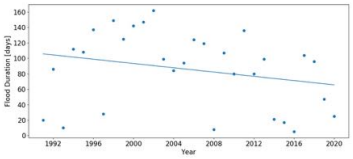

(f) Overall flood duration at Neak Luong.

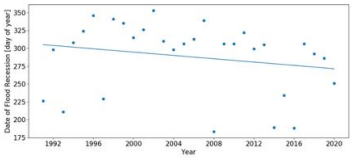

(g) Date of flood recession at Neak Luong.

Figure 11: Results of hydrological analysis at Neak Luong, short time series.

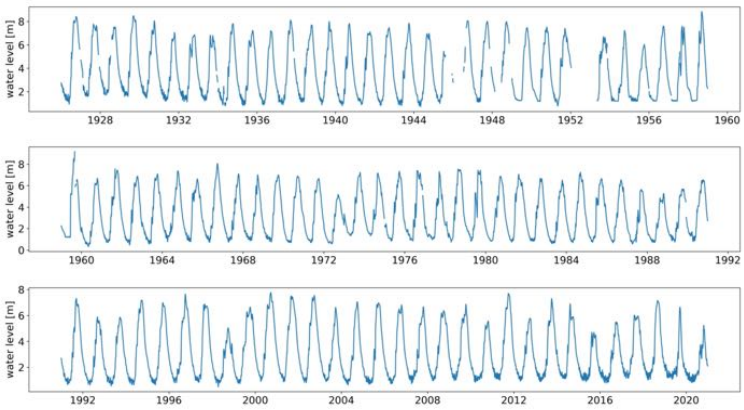

(a) Water levels at Neak Luong 1926-present.

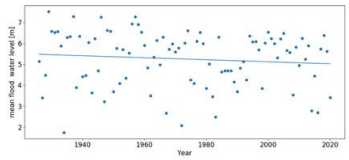

(b) Mean flood water levels at Neak Luong.

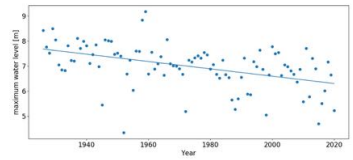

(c) Maximum water level at Neak Luong.

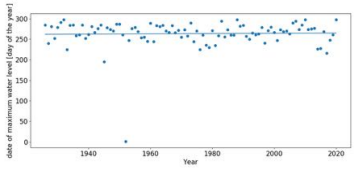

(d) Date of maximum water level at Neak Luong.

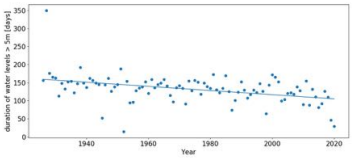

(e) Flood duration over 5 m at Neak Luong.

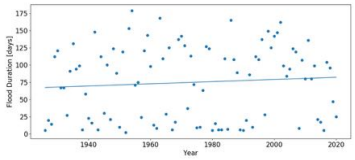

(f) Overall flood duration at Neak Luong.

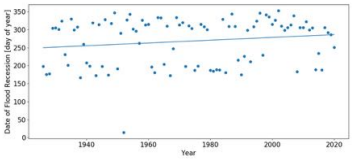

(g) Date of flood recession at Neak Luong.

Figure 12: Results of hydrological analysis at Neak Luong, long time series.

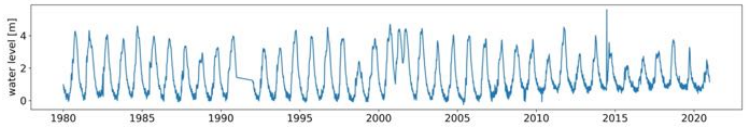

(a) Water levels at Tan Chau 1980-present.

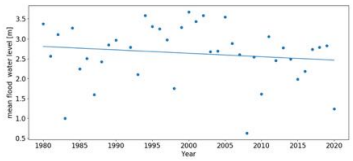

(b) Mean flood water levels at Tan Chau.

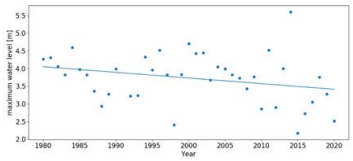

(c) Maximum water level at Tan Chau.

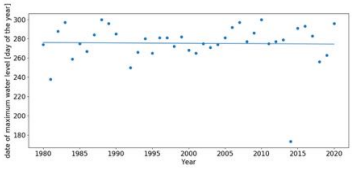

(d) Date of maximum water level at Tan Chau.

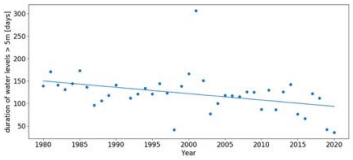

(e) Flood duration over 2 m at Tan Chau.

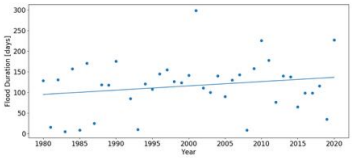

(f) Overall flood duration at Tan Chau.

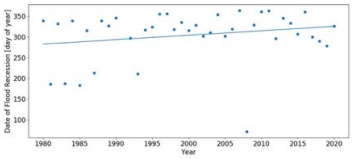

(g) Date of flood recession at Tan Chau.

Figure 13: Results of hydrological analysis at Tan Chau.

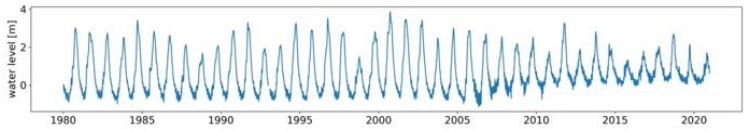

(a) Water levels at Chau Doc 1980-present.

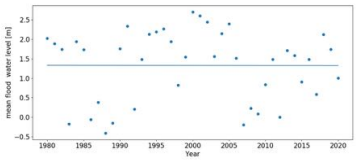

(b) Mean flood water levels at Chau Doc.

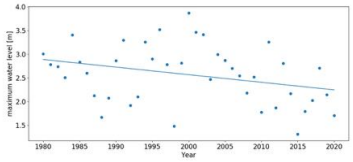

(c) Maximum water level at Chau Doc.

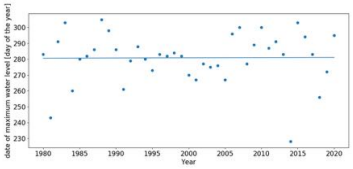

(d) Date of maximum water level at Chau Doc.

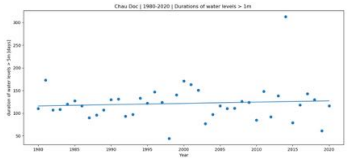

(e) Flood duration over 2 m at Chau Doc.

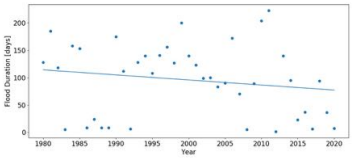

(f) Overall flood duration at Chau Doc.

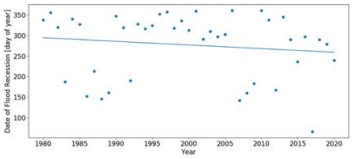

(g) Date of flood recession at Chau Doc.

Figure 14: Results of hydrological analysis at Chau Doc.

Appendix E: Results of the Detection of Inundation Extents Using Sentinel 1 and 2 and the Lamagat Correlation

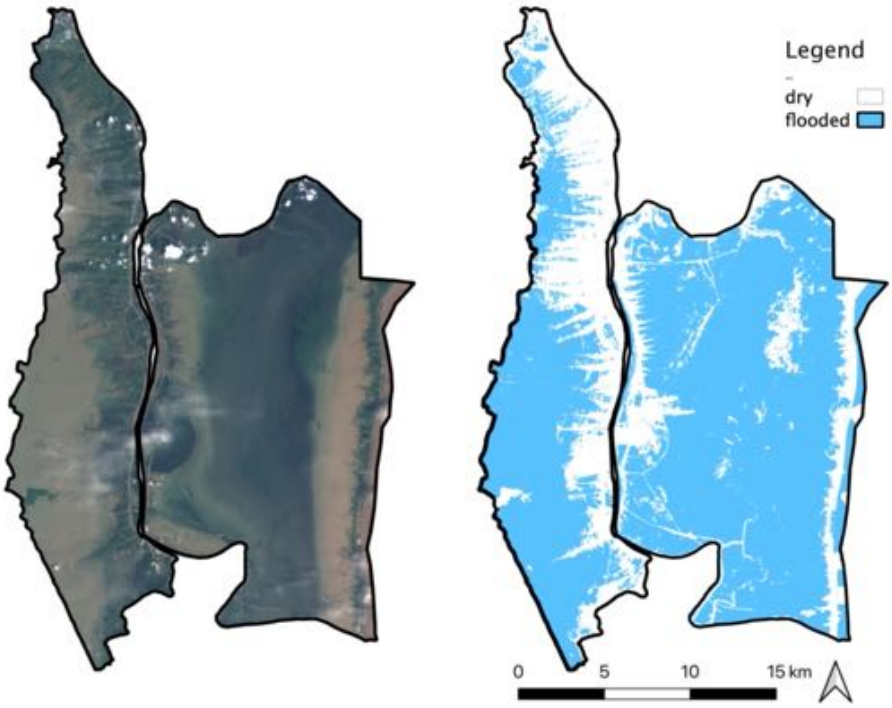

Figure 15: Example of classification using k-means and optical Sentinel data on 2018-10-01

Validation Date	Overall Accuracy Optical	Overall Accuracy Radar	Kappa Optical	Kappa Radar
2017-01-29	0.994	0.984	0.948	0.83
2018-06-24	0.938	0.979	0.757	0.908
2019-09-27	0.993	0.997	0.945	0.993
2019-08-14	0.917	0.917	0.526	0.371
Average	0.961	0.97	0.794	0.776
	0.965		0.785	

Table 3: Accuracy assessment of the inundation classification using Sentinel-1 and 2

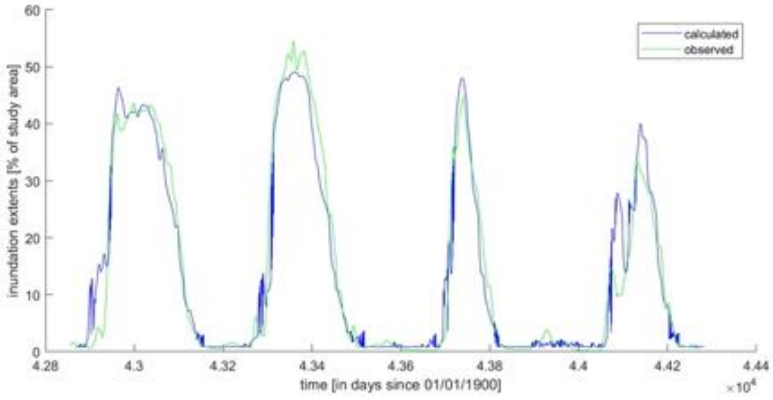

Figure 16: Observed inundation extents and extents calculated from upstream water levels using the Lamagat model, Zone A.

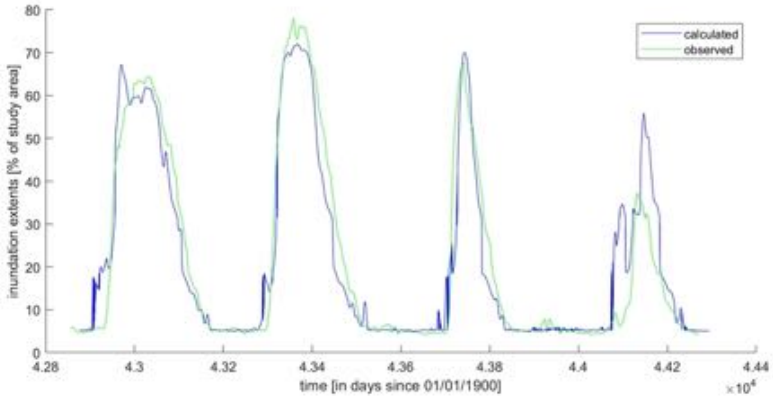

Figure 17: Observed inundation extents and extents calculated from upstream water levels using the Lamagat model, Zone B.

Water Level [m]	Optimal Delay Time
0.67	1
0.87	13.75
0.98	8.75
1.07	8.75
1.15	12.75
1.22	14.75
1.31	11.75
1.41	12.75
1.58	7.75
1.81	18.75
2.05	27.75
2.44	14.75
2.81	17.75
3.17	17.75
3.74	19.75
4.30	11.75
5.14	13.75
5.82	12.75
6.44	15.75

Table 4: Optimal correlation times by water level, Zone A

Water Level [m]	Optimal Delay Time
0.67	2.75
0.87	24.75
0.98	23.75
1.07	23.75
1.15	12.75
1.22	22.75
1.31	28.75
1.41	29.75
1.58	29.75
1.81	29.75
2.05	29.75
2.44	24.75
2.81	19.75
3.17	22.75
3.74	27.75
4.30	23.75
5.14	20.75
5.82	20.75
6.44	21.75

Table 5: Optimal correlation times by water level, Zone B

Appendix F: Comparison With Sentinel, Landsat, and TanDEM-X

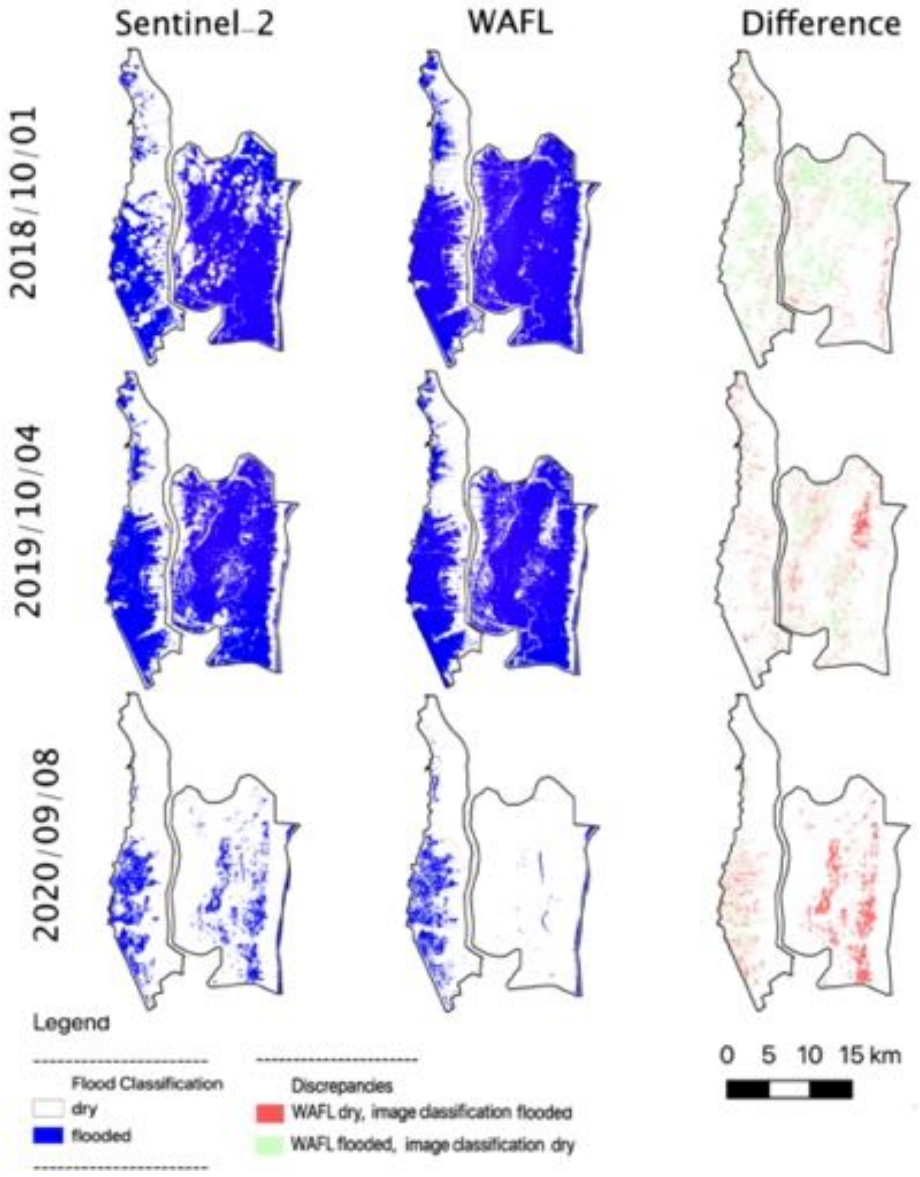

Figure 18: Comparison of WAFL-derived inundation extents, and extents directly derived from Sentinel-2 images in 2018, 2019, and 2020.

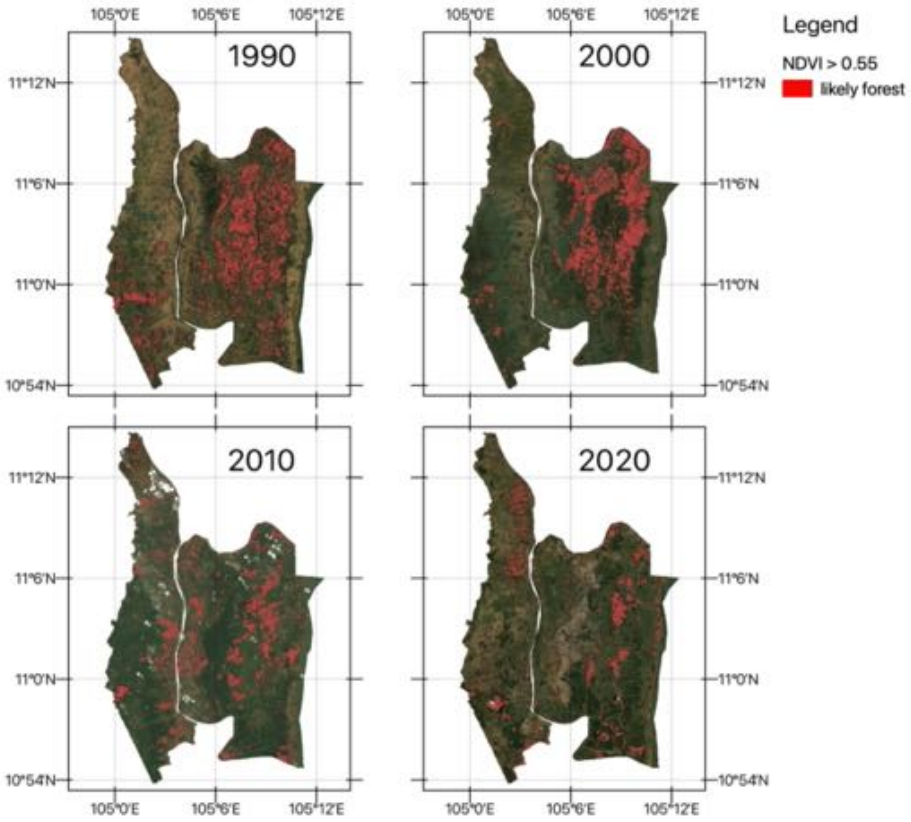

Figure 19: Distribution of natural vegetation in the early 1990s, 2000s, 2010s, and present.

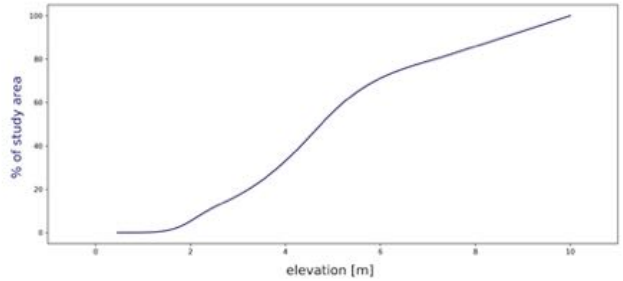

(a) Elevation-area curve Zone A

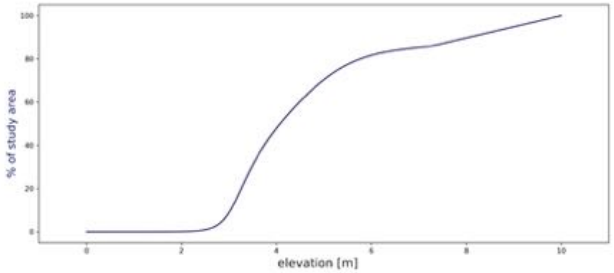

(b) Elevation-area curve Zone B

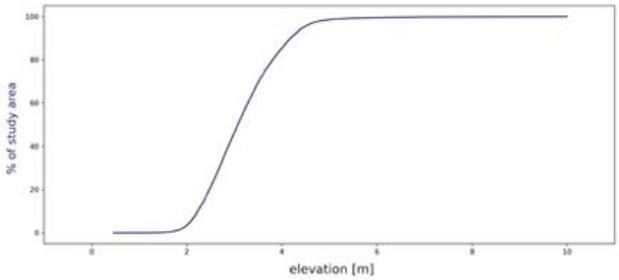

(c) Elevation-area curve in the 1km-radius around the logger in Zone A

Figure 20: Elevation-area curves according to TanDEM

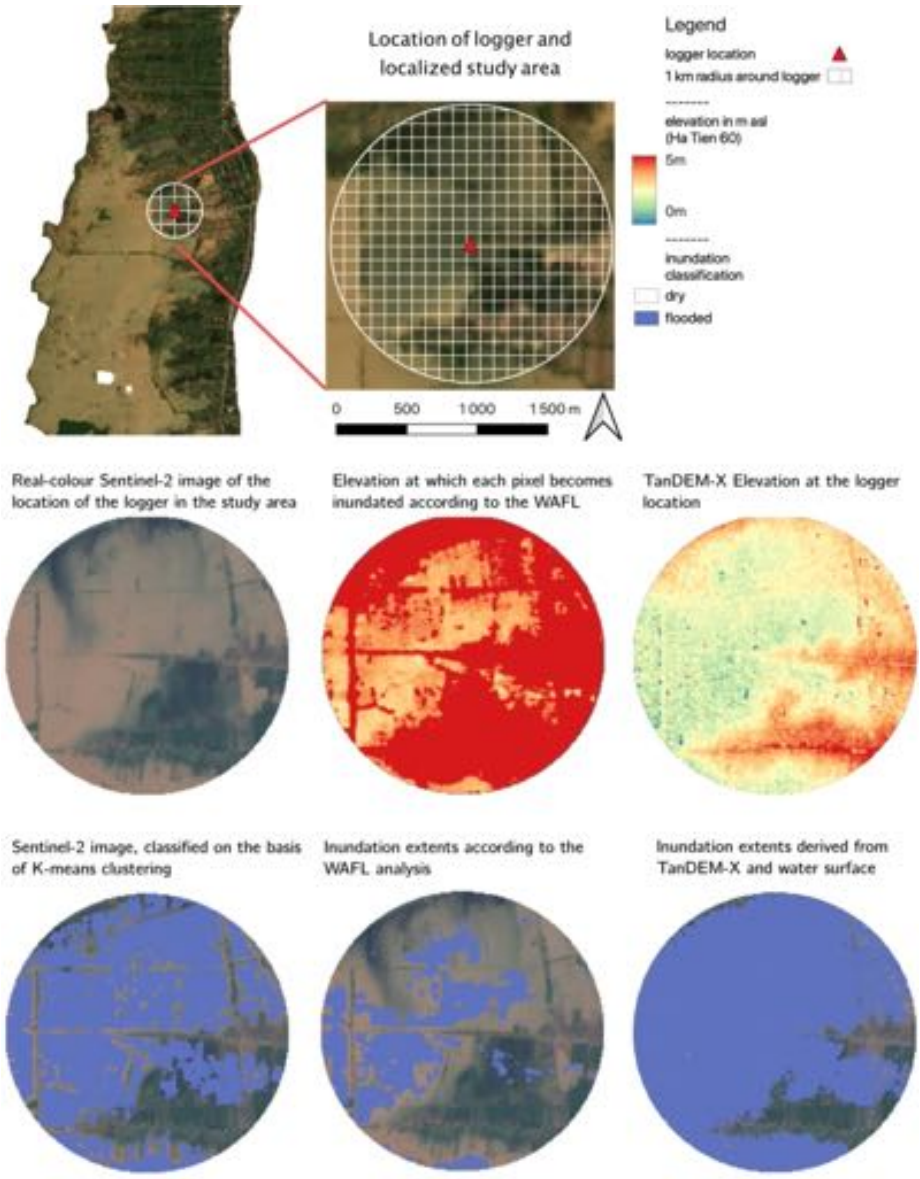

Figure 21: Local comparison of TanDEM-X-derived flood extent and WAFL-derived flood extent observed through Sentinel images.

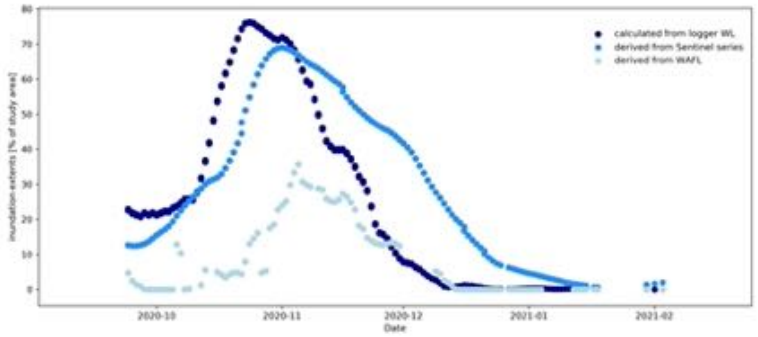

(a) Percentage of flooded area in the 1 km radius around the in-situ logger at Prek Chann West (PCW), derived from Sentinel, and calculated via the elevation-area curve of the TanDEM-X and WAFL.

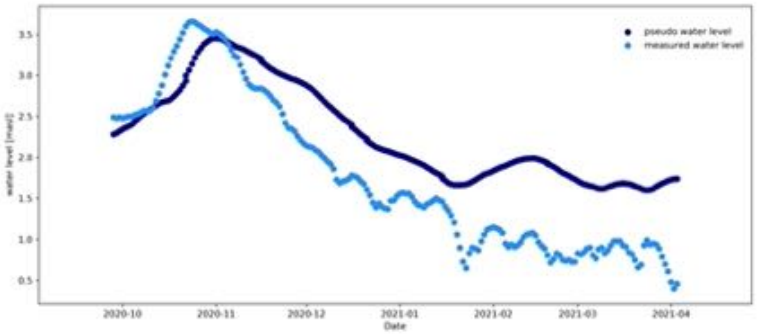

(b) Comparison of the pseudo-water-level calculated from the remote sensing observations and the TanDEM-X elevation-area curve, and the values measured by the in-situ logger

Figure 22: Comparison of DEM with local water level data.

Appendix G: Results of Analysis of Changes in Inundation Patterns in the Cambodian Mekong Delta

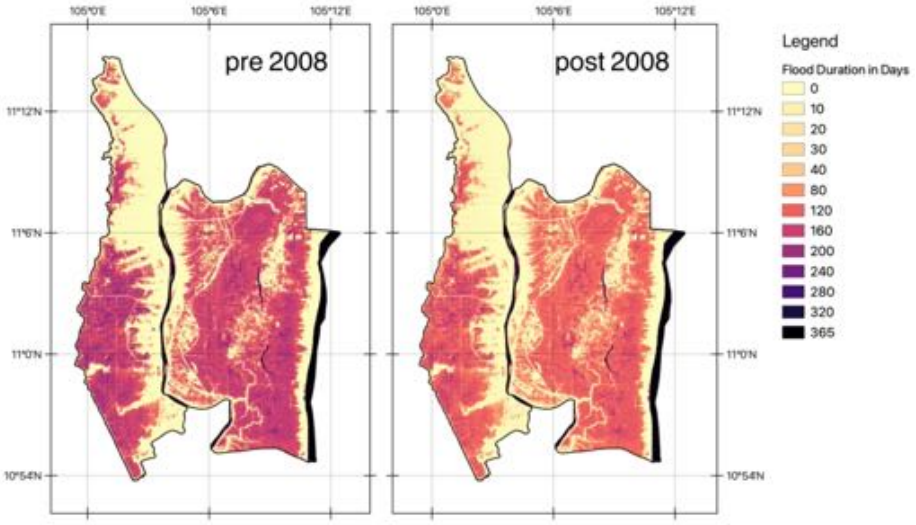

Figure 23: Change in inundation durations pre- and post-2008